SARS-CoV-2 infects brain astrocytes of COVID-19 patients and impairs neuronal viability

Fernanda Crunfli[1#], Victor Corasolla Carregari[1#], Flavio Protasio Veras[2,3#], Pedro Henrique Vendramini[1#], Aline Gazzola Fragnani Valença[1], André Saraiva Leão Marcelo Antunes[1], Caroline Brandão-Teles[1], Giuliana da Silva Zuccoli[1], Guilherme Reis-de-Oliveira[1], Lícia C.Silva-Costa[1], Verônica Monteiro Saia-Cereda[1], Ana Campos Codo[4], Pierina Lorencini Parise[5], Daniel A. Toledo Teixeira[5], Gabriela Fabiano de Souza[5], Stéfanie Primon Muraro[5], Bruno Marcel Silva Melo[2,3], Glaucia M. Almeida[6], Egidi Mayara Silva Firmino[3], Raíssa Guimarães Ludwig[7], Gabriel Palermo Ruiz[7], Thiago Leite Knittel[7], Gustavo Gastão Davanzo[4], Jaqueline Aline Gerhardt[7], Patrícia Brito Rodrigues[8], Julia Forato[5], Mariene Ribeiro Amorim[5], Natália Brunetti Silva[9], Matheus Cavalheiro Martini[5], Maíra Nilson Benatti[10], Sabrina Batah[10], Li Siyuan[10], Rafael Elias Marques Pereira Silva[11], Rafael Batista João[12], Lucas Scardua Silva[12], Mateus Henrique Nogueira[12], Ítalo Karmann Aventurato[12], Mariana Rabelo de Brito[12] Marina Koutsodontis Machado Alvim[12], José Roberto da Silva Júnior[13], Lívia Liviane Damião[13], Maria Ercilia de Paula Castilho Stefano[13], Iêda Maria Pereira de Sousa[13], Elessandra Dias da Rocha[13], Solange Maria Gonçalves[13], Luiz Henrique Lopes da Silva[13], Vanessa Bettini[13], Brunno Machado de Campos[12], Guilherme Ludwig[14], Rosa Maria Mendes Viana[15,16], Ronaldo Martins[15,16], Andre S. Vieira[17], José Carlos Alves-Filho[2,3], Eurico Arruda[15,16], Adriano S. Sebollela[6], Fernando Cendes[12], Fernando Queiroz Cunha[2,3], André Damásio[7,18], Marco Aurélio Ramirez Vinolo[8,18,19], Carolina Demarchi Munhoz[20], Stevens K. Rehen[21,22], Thais Mauad[23], Amaro Nunes Duarte-Neto[23], Luiz Fernando Ferraz da Silva[23], Marisa Dolhnikoff [23], Paulo Saldiva[23], Alexandre Todorovic Fabro[10], Alessandro S. Farias[9,18,19,21], Pedro Manoel M. Moraes-Vieira[4,18,19], José Luiz Proença Módena[5], **Clarissa Lin Yasuda[12*], Marcelo A. Mori[7,18,19*], Thiago Mattar Cunha[2,3*], Daniel Martins-de-Souza[1,18,24,25,*].**

1-Laboratory of Neuroproteomics, Department of Biochemistry and Tissue Biology, Institute of Biology, University of Campinas (UNICAMP), Campinas, São Paulo, Brazil;

2-Center for Research in Inflammatory Diseases (CRID), Ribeirão Preto Medical School (FMRP), University of São Paulo (USP), Ribeirão Preto, São Paulo, Brazil;

3-Department of Pharmacology, Ribeirão Preto Medical School (FMRP), University of São Paulo (USP), Ribeirão Preto, São Paulo, Brazil;

4-Laboratory of Immunometabolism, Department of Genetics, Evolution, Microbiology and Immunology, Institute of Biology, University of Campinas (UNICAMP), São Paulo, Brazil;

5- Laboratory of Emerging Viruses, Department of Genetics, Evolution, Microbiology and Immunology, Institute of Biology, University of Campinas (UNICAMP), São Paulo, Brazil;

6- Department of Biochemistry and Immunology, Ribeirão Preto Medical School (FMRP), University of São Paulo (USP), Ribeirão Preto, São Paulo, Brazil;

7- Department of Biochemistry and Tissue Biology, Institute of Biology, University of Campinas (UNICAMP), Campinas, São Paulo, Brazil;

8- Laboratory of Immunoinflammation, Department of Genetics, Microbiology and Immunology, Institute of Biology, University of Campinas (UNICAMP), Campinas, São Paulo, Brazil;

9- Autoimmune Research Laboratory, Department of Genetics, Microbiology and Immunology, Institute of Biology, University of Campinas (UNICAMP), Campinas, São Paulo, Brazil;

10- Department of Pathology and Legal Medicine, Ribeirão Preto Medical School (FMRP), University of São Paulo (USP), Ribeirão Preto, São Paulo, Brazil;

11- Brazilian Biosciences National Laboratory (LNBio), Campinas, São Paulo, Brazil;

12- Laboratory of Neuroimaging, Department of Neurology, University of Campinas (UNICAMP), Campinas, São Paulo, Brazil;

13- Department of Radiology, Clinical Hospital, University of Campinas (UNICAMP), Campinas, São Paulo, Brazil;

14- Institute of Mathematics, Statistics and Scientific Computation,.University of Campinas (UNICAMP), Campinas, São Paulo, Brazil;

15- Virology Research Center, Ribeirão Preto Medical School (FMRP), University of São Paulo (USP), Ribeirão Preto, São Paulo, Brazil;

16- Department of Cell and Molecular Biology, Ribeirão Preto Medical School (FMRP), University of São Paulo (USP), Ribeirão Preto, São Paulo, Brazil.

17- Department of Animal Biology, Institute of Biology, University of Campinas (UNICAMP), Campinas, São Paulo, Brazil;

18- Experimental Medicine Research Cluster (EMRC), University of Campinas (UNICAMP), Campinas, São Paulo, Brazil;

19- Obesity and Comorbidities Research Center (OCRC), University of Campinas (UNICAMP), Campinas, São Paulo, Brazil;

20- Department of Pharmacology, Institute of Biomedical Science, University of São Paulo, São Paulo, Brazil

21- D'Or Institute for Research and Education (IDOR), Rio de Janeiro, Brazil;

22- Institute of Biomedical Science (ICB), Federal University of Rio de Janeiro (UFRJ), Rio de Janeiro, Brazil;

23- Department of Pathology, School of Medicine (FM), University of São Paulo (USP), São Paulo, Brazil;

24- National Institute for Biomarkers in Neuropsychiatry (INBioN), Brazilian National Council for Scientific and Technological Development (CNPq), Brazil;

25- D'Or Institute for Research and Education (IDOR), São Paulo, Brazil;

 # These authors contributed equally to this work.

***Correspondence should be addressed to:**

Daniel Martins-de-Souza, PhD: dmsouza@unicamp.br

Thiago Mattar Cunha, PhD: thicunha@fmrp.usp.br

Marcelo A. Mori, PhD: morima@unicamp.br

Clarissa Lin Yasuda, MD, PhD: cyasuda@unicamp.br

Abstract

COVID-19 patients may exhibit neuropsychiatric and/or neurological symptoms. We found that anxiety and cognitive impairment are manifested by 28-56% of SARS-CoV-2-infected individuals with mild or no respiratory symptoms and are associated with altered cerebral cortical thickness. Using an independent cohort, we found histopathological signs of brain damage in 19% of individuals who died of COVID-19. All of the affected brain tissues exhibited foci of SARS-CoV-2 infection, particularly in astrocytes. Infection of neural stem cell-derived astrocytes changed energy metabolism, altered key proteins and metabolites used to fuel neurons and for biogenesis of neurotransmitters, and elicited a secretory phenotype that reduces neuronal viability. Our data support the model where SARS-CoV-2 reaches the brain, infects astrocytes and triggers neuropathological changes that contribute to the structural and functional alterations in the brain of COVID-19 patients.

Main text

COVID-19 is a disease caused by infection with the severe acute respiratory syndrome coronavirus 2 (SARS-CoV-2). Although the most commonly observed symptoms of COVID-19 are respiratory and related to pulmonary infection, a growing body of evidence has demonstrated that SARS-CoV-2 may have extrapulmonary effects [1]. Notably, over 30% of COVID-19 patients manifest neurological and even neuropsychiatric symptoms [2,3], eventually presenting some degree of encephalitis [4]. More than half of these patients continue to exhibit neurological symptoms even three months after the onset of the disease, when the virus is no longer detected [5]. This is consistent with substantial damage to the nervous system [6].

To explore the extent of brain damage in COVID-19 patients, we performed cortical surface-based morphometry analysis using high-resolution 3T MRI of 81 subjects diagnosed with COVID-19 who had mild respiratory symptoms and did not require hospitalization or oxygen support. The analysis was performed within a median interval of 54 days after SARS-CoV-2 detection by RT-qPCR and the subjects were compared to 145 healthy volunteers (Supplementary Table 1 and 2). The analysis revealed areas of reduced cortical thickness in the left lingual gyrus, calcarine sulcus - including the cuneus - and olfactory sulcus - including the rectus gyrus (Fig. 1a). In contrast, increased thickness was detected in the central sulcus - including the precentral and postcentral gyrus - and superior occipital gyrus (Fig. 1a), which can be associated with vasogenic edemas [7]. A subgroup of these individuals (n = 61) were subjected to neuropsychological evaluation for anxiety (Beck Anxiety Inventory, BAI), depression (Beck Depression Inventory, BDI), logical memory (Wechsler Memory Scale), cognitive functions (TRAIL Making Test) and fatigue (Chalder Fatigue Questionnaire, CFQ). These tests were performed between 21 and 120 days after diagnosis (median of 59 days). Symptoms of anxiety were identified in approximately 28% of the subjects, and 20% of individuals presented symptoms of depression (Supplementary Fig. 1a). Abnormal performances were observed in nearly 28% of participants on logical memory and approximately 34% and 56% on TRAIL A and B, respectively (Supplementary Table 3 and Supplementary Fig. 1b). We also correlated the changes in cortex thickness with the neuropsychological evaluation. We identified a negative correlation between BAI and cortical thickness of orbitofrontal regions (adjusted for CFQ) (Fig. 1b and Supplementary Table 4) and a positive correlation between TRAIL B and cortical thickness of the right gyrus rectus (Fig. 1c and Supplementary Table 5). We also found partial correlations between logical memory (immediate recall, adjusted for BAI, BDI and CFQ) and

cortical thickness of regions associated with language (Supplementary Table 6). These results suggest that a thinner cortex in these areas is associated with poor performance on this verbal memory task. Overall, our findings evidence major alterations in brain cortex structure associated with neuropsychiatric symptoms as a consequence of COVID-19.

Brain alterations in COVID-19 patients could be a consequence of inflammatory or hemodynamic changes secondary to peripheral infection or could be caused by the ability of SARS-CoV-2 to invade the central nervous system (CNS) and compromise cell viability and brain function. Although exacerbated inflammation and cardiovascular dysfunction have been well characterized in COVID-19 patients [8], infection of the CNS by SARS-CoV-2 remains under debate. We performed a minimally invasive autopsy via endonasal trans-ethmoidal access of brain samples from 26 individuals who died of COVID-19 and analyzed histopathological features. We found alterations consistent with necrosis and inflammation in 19% of the brain tissues from these individuos (5/20) (Fig. 2a and Supplementary Fig. 2a). Notably, SARS-CoV-2 genetic material and spike protein was detected in all of these five samples (Fig. 2b,c). SARS-CoV-2 spike protein was found in about one third of the cells in one of the slices of brain tissue analyzed (Fig. 2d), the majority of these cells being astrocytes (Fig. 2e). We also found the virus in neurons (Supplementary Fig. 2b), but not in microglia (Supplementary Fig. 2c). The presence of SARS-CoV-2 spike protein correlated with the presence of double-stranded RNA (dsRNA) in the infected cells (Fig. 2f), indicating replicative virus in the brain tissue.

We have also conducted liquid chromatography-mass spectrometry (LC/MS)-based shotgun proteomics with a different set of samples, consisting of 12 *postmortem* brain samples from COVID-19 patients vs. 8 SARS-CoV-2-negative controls. We identified 119 differentially expressed proteins with the most highly enriched pathways being associated with

neurodegenerative diseases and carbon metabolism (Fig. 2g). Moreover, astrocyte proteins were enriched among the differentially expressed proteins, consistent with the higher frequency of infected astrocytes (Fig. 2h).

In order to investigate the consequences of SARS-CoV-2 infection on astrocytes, we generated human neural stem cell-derived astrocytes, exposed them to the virus for 1h, and analyzed cell response after 24h. We confirmed that SARS-CoV-2 is able to infect human astrocytes (Fig. 3a-c). Notably, we also found the presence of dsRNA in SARS-CoV-2-infected astrocytes i*n vitro*, but not in mock control cells (Fig. 3a-c). Altogether these results indicate that astrocytes are permissive cells for SARS-CoV-2 infection and represent a site for virus replication in the central nervous system.

In an attempt to identify downstream mechanisms triggered by SARS-CoV2 infection and possibly involved in the pathophysiology of COVID-19, we employed an unbiased proteomic analysis of infected astrocytes. LC/MS-based proteomics revealed 233 differentially expressed proteins in SARS-CoV-2-infected astrocytes compared to mock control cells. A group of approximately 50 proteins formed a molecular signature which distinguished infected astrocytes from controls (Fig. 4a). Pathway enrichment analysis revealed that these proteins are involved in a wide range of biological processes (Fig. 4b). When we compared these pathways to those normally enriched in brain proteomics, we found carbon metabolism, glycolysis/gluconeogenesis, biosynthesis of amino acids, pentose phosphate pathway and necroptosis in common (Fig. 4c). In agreement, LC/MS-based metabolomic analysis of SARS-CoV-2-infected astrocytes showed marked changes in metabolic intermediates of glycolysis, the TCA cycle and anaplerotic reactions, indicating extensive remodeling of astrocyte metabolism (Supplementary Fig. 3). This phenomenon was marked by the decrease in pyruvate

and lactate, which are downstream metabolites of the glycolytic pathway, as well as a reduction in glutamine and intermediates of glutamine metabolism such as glutamate, GABA and alpha-ketoglutarate (Fig. 4d). Astrocyte bioenergetics were further characterized by Seahorse Extracellular Flux analysis, showing increased respiration in infected cells (Fig. 4e and Supplementary Fig. 4). Together, these results demonstrate increased metabolic activity in SARS-CoV-2-infected astrocytes and a reduction of metabolites used by these cells to support neuronal metabolism.

These observations prompted us to investigate whether neuronal viability could be indirectly affected by infection of astrocytes with SARS-CoV-2. To test that, we cultured differentiated SH-SY5Y neurons with the conditioned medium of SARS-CoV-2-infected astrocytes. SH-SY5Y cells are more closely related to adrenergic neurons, but they also express dopaminergic markers [9]. As observed in Fig. 4f, conditioned medium of SARS-CoV2-infected astrocytes induced apoptosis in SH-SY5Y neurons. These results suggest that the infection of astrocytes by SARS-CoV-2 might be a trigger event to reduce neuronal viability.

This study and other reports showing alterations in brain structure and the manifestation of neurological symptoms in COVID-19 patients [10,11] have raised a debate on whether these clinical features are consequence of peripheral changes or rather the potential ability of the virus to invade the CNS. Our findings support the latter, at least in part, as we found SARS-CoV-2 in the brain tissue collected from patients who died of COVID-19. The potential of SARS-CoV-2 to infect brain cells has been demonstrated using *in vitro* models such as stem cell-derived neural cells and cerebral organoids [12]. Viral particles have also been found in the brain [13], localized in the microvasculature and in neurons [12], as well as in the choroid plexus[14] and meninges [15]. However, the magnitude of this infection and its distribution in the brain tissue had not been

demonstrated. We show that SARS-CoV-2 may infect almost one third of the cells in the brain and the majority of these cells are astrocytes.

In astrocytes, SARS-CoV-2 infection results in marked changes in cellular metabolism. Since astrocyte metabolism is key to support neuronal function, we hypothesized that these changes could indirectly impact neurons. Astrocytes support neurons metabolically by exporting lactate [16]. One of the most critical alterations caused by SARS-CoV-2 infection in astrocytes is the decrease in pyruvate and lactate levels. In spite of these intracellular changes, lactate is not altered in the conditioned medium of SARS-CoV-2-infected astrocytes (Supplementary Fig. 5), suggesting that infected astrocytes divert pyruvate to lactate production and export it to preserve neuronal metabolism; however, in order to sustain its own metabolism, carbon sources other than the ones derived from glucose would have to be used to fuel the TCA cycle. Supporting this notion, intermediates of glutamine metabolism such as glutamate and GABA are decreased in SARS-CoV-2-infected astrocytes, suggesting that glutaminolysis is being used as an alternative source of carbons to fuel astrocyte oxidative metabolism. Importantly, astrocyte-derived glutamine is required for neuronal synthesis of the neurotransmitters glutamate and GABA [17]. Astrocytes play a vital role in neurotransmitter recycling, a crucial process for the maintenance of synaptic transmission and neuronal excitability. This is especially important for glutamatergic synapses since proper glutamate uptake by astroglia prevents the occurrence of excitotoxicity [18]. Upon this uptake, glutamine synthetase converts glutamate to glutamine, which can then be transferred back to neurons, thus closing the glutamate-glutamine cycle. This is also true for GABAergic synapses, where the neurotransmitter GABA is taken up by astrocytes and metabolized first to glutamate and then to glutamine [19]. Moreover, astrocytes are responsible for maintaining glutamate levels in the brain. Hence, given the importance of the coupling between

astrocytes and neurons, astrocytic alterations in glutamine metabolism are expected to compromise neuronal function, affecting synaptic function and plasticity [20].

We also found that SARS-CoV-2 infection elicits a secretory phenotype in astrocytes that results in increased neuronal apoptosis. Neuronal death may explain, at least partially, the alterations in cortical thickness found in COVID-19 patients. A recent study with 60 recovered patients and 39 healthy controls also identified gray matter abnormalities 97 days after the onset of the disease, with increased volume in some areas of the brain [5]. While that study analyzed hospitalized patients, we evaluated individuals that did not have to be hospitalized (i.e. had mild respiratory symptoms), and nevertheless, we observed notable alterations of cortical thickness. Importantly, some of these alterations correlated with symptoms of anxiety and impaired cognition, which is consistent with previous literature [21,22]. Since one of the hypotheses for the neuroinvasive mechanism of SARS-CoV-2 is via the olfactory nerves [23], we speculate that the associations between BAI and TRAIL B scores and structural alterations in the orbitofrontal region may be a result of the action of the virus in this cortical area, closely related to the olfactory nerves.

Our findings are consistent with a model in which SARS-CoV-2 is able to reach the central nervous system of COVID-19 patients, infects astrocytes and secondarily impairs neuronal function and viability. These changes are likely to contribute to the alterations of brain structure as observed here and elsewhere, thereby resulting in the neurological and neuropsychiatric symptoms manifested by some COVID-19 patients. Our study comes as a cautionary note that interventions directed to treat COVID-19 should also envision ways to prevent SARS-CoV-2 invasion of the CNS and/or replication in astrocytes.

Material and Methods

Brain imaging and neuropsychological evaluation

Participants

Eighty-one patients (60 women, median 37 years of age) previously infected with SARS-CoV-2 were enrolled prospectively for this study after signing an informed consent form approved by the local Ethics Committee. These individuals presented mild symptoms during the acute phase and did not require hospitalization or oxygen therapy. They had a median interval of 54 days (range 16-120 days) between their RT-PCR exam and the day of MRI scanning and interview. For cortical thickness analysis, we included one hundred and forty-five controls (103 women, median 38 years of age) [24] from our Neuroimaging databank, given the difficulties and risk of recruiting healthy volunteers during the pandemic. The outpatients and healthy controls were balanced for age (p=0.45) and sex (p=0.65). The neuropsychological evaluations and neuroimaging analyses were approved by the Research Ethics Committee of the University of Campinas (CAAE: 31556920.0.0000.5404) and all subjects signed a consent form to participate.

Neuropsychological evaluation

We performed neuropsychological evaluations of sixty-one of these patients. They were tested for symptoms of anxiety using the Beck Anxiety Inventory (BAI) and symptoms of depression using the Beck Depression Inventory (BDI) [25]. Symptoms of anxiety were confirmed for those with a BAI higher than 10 points, and depression symptoms defined for those with minimum of 14 points on the BDI. In terms of depression, subjects were categorized with mild

(BDI 14-19), moderate (20-35) and severe (36-63) symptoms. Anxiety symptoms were considered mild (BAI 11-19), moderate (20-30) and severe (31-63). We evaluated verbal memory (immediate and delayed episodic memory) using the Logical Memory subtest from the Wechsler Memory Scale (WMS-R) [26], in which the examiner verbally presents two stories, and each story includes 25 pertinent pieces of information. Subjects are required to recall details of each story immediately after its presentation and again after 20 minutes. To evaluate other cognitive functions, we applied the TRAIL Making Test (TMT) , which is subdivided into two steps. *Step A* assesses processing speed and visual search in a task that requires ascending connection order of 25 numbers, randomly arranged. *Step B* evaluates alternating attention and cognitive flexibility in a task associated with shifting rules in an ascending sequence of 25 numbers. A training stage is applied to both steps. We calculated z-scores for the results of these tests based on Brazilian normative data [26,27]. For each test, the function was categorized as: "preserved" if the z-score was higher than -0.99; "below average" when the z-score was between -1 and -1.49; "minor impairment" if the z-score was between -1.5 and -1.99; and "major impairment" for z-score values equal to or lower than -2. The Chalder Fatigue Questionnaire (CFQ-11) [28] was used to evaluate fatigue in these subjects; they were instructed to answer 11 questions (measured on a Likert scale 0-3), which yields a global score out of 33.

Neuroimaging analysis

We obtained the structural, 3D, T1-weighted images from a 3T Achieva-Philips MRI scanner (voxel size: 1x1x1 mm, TE = 3.2 ms, TR = 7 ms, matrix = 240x240x180, flip angle = 8 and FOV = 240x240 mm2) [24,25]. We performed imaging analysis with the CAT12 toolbox (http://www.neuro.uni-jena.de/cat/, version r1711) within SPM12 (http://www.fil.ion.ucl.ac.uk/spm/, version 7487) using MATLAB 2017b to extract Cortical

Thickness (CT) maps, according to the default parameters. The T1 images were initially spatially registered and segmented into gray matter, white matter and cerebrospinal fluid. Finally, we calculated the cortical thickness using the projection method described by Dahnke et al. [29]. For voxelwise analysis of extracted maps, we used CAT12/SPM12 tools for an independent T-test (comparing COVID-19 patients and healthy controls), including age and sex as covariates. The results displayed were corrected for multiple comparisons using False Discovery Rate (FDR) [30] correction ($p<0.05$). For anatomical identification, we used the "Destrieux Atlas 2009" [31]. Cortical parcellation was performed with standard CAT12 tools to extract the cortical thickness of regions of interest for correlations with neuropsychological scores. We used SPSS 22 for statistical analysis of clinical and neuropsychological variables. The FDR procedure was applied to adjust p-values for multiple comparisons (when necessary) with R software [32].

Postmortem brain samples from COVID-19

Twenty-six individuals who died from complications related to COVID-19 were autopsied with an ultrasound-guided, minimally invasive approach using endonasal trans-ethmoidal access. Brain tissue samples were collected and fixed using a 10% neutral buffered formalin solution. After fixation, the tissue was embedded in a paraffin block and sectioned into slices with a thickness of 3 μm. The sections were stained by H&E and immunofluorescence. For proteomic analysis, twelve COVID-19 patients were autopsied using the same approach. Brain tissue samples were collected and macerated in lysis buffer (100 mM Tris-HCl, pH 8.0, 150 mM NaCl, 1 mM EDTA, 0.5% Triton X-100) prior to trypsin digestion. The autopsy studies were approved by the National Commission for Research Ethics (CAAE: 32475220.5.0000.5440 and CAAE: 38071420.0.1001.5404).

Generation of human astrocytes (hES-derived)

Differentiation of glial progenitor cells was performed from neural stem cells (NSC) derived from pluripotent human embryonic stem cells (hES, cell line BR-1) [33], according to the method published by Trindade, 2020 [34]. NSCs were cultured in plates coated with Geltrex Matrix (Thermo Fisher Scientific, MA, USA) using 1:1 Neurobasal™/Advanced DMEM/F12 medium and 2% neural induction supplement. Upon reaching 50% confluence, the medium was changed to DMEM/F12, 1% N2 supplement, 1% fetal bovine serum (FBS), and 1% Penicillin-Streptomycin and maintained at 37°C in humidified air with 5% CO_2 for 21 days. At this stage, cells were considered glial progenitor cells (GPCs). Subsequently, GPCs were plated at low density (30-40% confluence) on Geltrex coated plates and treated with DMEM/F12 medium, 1% GlutaMAX Supplement, 10% FBS and 1% penicillin-streptomycin. The differentiation medium was replaced every 2-3 days. After 4 weeks of differentiation, the cells were considered mature astrocytes. The cells were plated on Geltrex-coated coverslips at a density of $4x10^4$ cells for immunostaining assays; and $25x10^4$ cells for viral load, proteomic and metabolomic analysis. All products used for cell culture are from Thermo Fisher Scientific, MA, USA.

Virus strain

The HIAE-02-SARS-CoV-2/SP02/human/2020/BRA (GenBank accession number MT126808.1) virus strain was used for all *in vitro* experiments. The virus was isolated from the first confirmed case of COVID-19 in Brazil and kindly donated by Prof. Dr. Edison Durigon

(ICB-USP). Viral stock was propagated in Vero CCL-81 cells (ATCC) cultivated in DMEM supplemented with 10% heat-inactivated FBS and 1% of penicillin and streptomycin, and incubated at 37°C with 5% CO_2 atmosphere. Viral titer was determined by the plaque-forming assay using Vero cells.

In vitro infection

Astrocytes were infected with SARS-CoV-2 for 1 hour using an MOI of 0.1 (proteomics, metabolomics, gene expression, viral load, bioenergetics assays and flow cytometer analysis) and 1 (immunostaining experiments) under gentle agitation at room temperature. After viral adsorption, cells were washed twice with phosphate-buffered saline (PBS) and incubated with DMEM/F12 supplemented with 10% FBS, 1% GlutaMAX and 1% penicillin and streptomycin for 24 hours at standard culture conditions (37ºC and 5% CO_2 atmosphere). Astrocytes cells were harvested according to the experiment: immunostaining, proteomics and metabolomic analysis, gene expression analysis and viral load, bioenergetics test and flow cytometer analysis.

Immunostaining and confocal microscopy

Brain sections from autopsies and astrocyte cell cultures were fixed with 10% neutral buffered formalin solution or 4% paraformaldehyde (PFA), respectively. Subsequently, the samples were incubated with primary antibodies: mouse monoclonal anti-GFAP Alexa Fluor 488 (EMD Millipore, clone GA5, cat. MAB3402X, 1:400), human chimeric monoclonal anti-SARS-CoV-2 Spike S1 (GeneScript, clone HC2001, cat. A02038, 1:500), rabbit polyclonal anti-SARS-CoV-2 Spike (Rhea Biotech, cat. IM-0828, 1:500), mouse monoclonal anti-double stranded RNA J2 (dsRNA, SCICONS English & Scientific Consulting Kft., clone J2-1909, cat.

10010200; 1:1,000), rabbit polyclonal anti-Iba1 (FUJIFILM Wako Pure Chemical Corporation, cat. 019-19741, 1:1,000) and rabbit monoclonal anti-NeuN (Abcam, clone EPR12763, cat. Ab128886, 1:1,000). The slides were washed twice with TBS-T (Tris-Buffered Saline with Tween 20) and incubated with secondary antibodies donkey anti-mouse IgG AlexaFluor 647 (Thermo Fisher Scientific; cat. A32787; 1:800) or AlexaFluor 488 (Abcam; cat. ab150061; 1:800), donkey anti-rabbit IgG AlexaFluor 488 (Abcam; cat. ab150065; 1:800) or AlexaFluor 594 (Abcam; cat. ab150076; 1:800) and goat anti-human IgG FITC (Rhea Biotech, cat. IC-3H04, 1:400). Controls were performed for secondary antibody fluorescence. Nuclei were stained with DAPI (Life Technologies; cat. D1306; 1:1,000). Images were acquired by an Axio Observer combined with an LSM 780 confocal device (Carl Zeiss) with 630x magnification and Z-stack (0.15µm) for brain sections. Colocalization analysis between GFAP and SARS-CoV-2 S1 or GFAP and dsRNA were quantified using the Fiji/ImageJ software. To determine colocalization, we used a ratio of GFAP:SARS-CoV-2 and GFAP:dsRNA in each sample by analyzing Pearson's correlation coefficient.

Proteomics sample preparation, LC-MS/MS analysis and data processing

Astrocytes infected with SARS-CoV-2 and a mock control were collected in biological triplicates. Cells were chemically lysed with Lysis Buffer: (100 mM Tris-HCl, 1 mM EDTA, 150 mM NaCl, 1% Triton-X, protease and phosphatase inhibitors) and mechanically lysed with an ultrasonication probe in 3 cycles of 20s each with 90% of frequency. The total protein extract was quantified by BCA, according to the manufacturer's instructions (Thermo Fisher Scientific, MA, USA). 30 µg of total protein extract from each sample was transferred to a Microcon-10 Centrifugal Filter, with 10 kDa cutoff, for FASP protein digestion [35]. Proteins were reduced (10 mM DTT), alkylated (50 mM IAA) and digested overnight by trypsin at 37°C in 50 mM

ammonium bicarbonate (AmBic), pH 8.0. One the following day, trypsin activity was quenched by adding formic acid (FA) to a final concentration of 1% (v/v) and the peptides were recovered from the filter in 50 mM AmBic, concentrated in a SpeedVac and stored at -80°C until use.

Digested peptides were resuspended in 0.1% FA. LC-MS/MS analysis was performed in an ACQUITY M-Class System (Waters Corporation, Milford, MA) coupled online to a Synapt G2-Si mass spectrometer (Waters Corporation, Milford, MA). 1 µg of peptides were loaded onto a trapping column (Symmetry C18 5 µm, 180 µm × 20 mm, Waters Corporation, Milford, MA) and subsequently separated in the analytical column (HSS T3 C18 1.8 µm, 75 µm × 150 mm; Waters Corporation, Milford, MA). For gradient elution, 0.1% FA was used as eluent A and Acetonitrile-FA (99.9% ACN:0.1% FA) as eluent B. Reversed phase gradient was carried out over 120 minutes, with a linear gradient 3 - 60% acetonitrile over 90 min at 300 nL/min. In the Synapt G2-Si, the peptide spectra were acquired by ion mobility-enhanced data-independent acquisition (HDMS^{e}). Mass spectrometry analysis was performed in "Resolution Mode", switching between low (4 eV) and high (25–60 eV) collision energies, using a scan time of 1.0 s per function over 50–2000 m/z. The wave velocity for ion mobility separation was 1.000 m/s and the transfer wave velocity was 175 m/s. A [Glu1]-Fibrinopeptide B Standard (Waters Corporation, Milford, MA) was used as the reference lock mass compound. Each sample was run in three technical replicates.

The raw data from each experiment were processed in Progenesis QI for proteomics (Waters Corporation, Milford, MA). Tandem mass spectra were searched against the *Homo sapiens* proteome database (UNIPROT Protein reviewed release 2020-04), using tolerance parameters of 20 ppm for precursor ions and 10 ppm for product ions. For peptide identification, carbamidomethylation of cysteines was set as a fixed modification, oxidation of methionines as a

variable modification, 2 missed cleavages, and a false discovery rate (FDR) < 1%. Protein identification was performed using a minimum of 1 fragment ion matched per peptide, a minimum of 3 fragment ions per protein and a minimum of 1 peptide per protein.

Label-free quantitative analysis was carried out using the relative abundance intensity normalized by all peptides identified. The expression analysis was performed considering the technical replicates for each experimental condition, following the hypothesis that each group is independent. Proteins with ANOVA (p) ≤ 0.05 between the groups were considered differentially expressed.

Metabolomics sample preparation, UPLC-MS/MS analysis and data processing

The medium was washed twice with PBS at physiologic pH, then the cells (10^6) were collected with 600 µL of methanol. Samples were dried and stored at -80 °C until the metabolite extraction step. Volumes of 473 µL of water, 600 µL of methanol, and 1168 µL of chloroform were added, and then the tubes were shaken vigorously for 2 minutes. Subsequently, samples were centrifuged for 5 minutes at 13,000 x g. The aqueous supernatant and the organic phase (lower phase) were collected and dried for 60 and 40 min (respectively) in a vacuum concentrator. All samples were stored at -80 °C until analysis by UPLC-MS/MS.

The samples were resuspended in 100 µL of methanol: water mixture (1:1) and for each analysis, 4 µL of the sample was injected. Sample separation was performed by hydrophobic interaction liquid chromatography (HILIC) using an Acquity UPLC® BEH amide column (1.7 µm, 2.1 mm x 100 mm). The mobile phases used for the separations were ACN: H_2O (80:20) as mobile phase A and ACN: H_2O (30:70) as mobile phase B, both phases containing 10 mM of ammonium formate and 0.1% of ammonium hydroxide. The separation was then performed by a

gradient from 99% to 1% buffer A over 7 min. The column was returned to 99% buffer A for 2 min for re-equilibration before the next injection for a total run time of 10 min. Data acquisition was performed in negative mode and the instrument was operated in MS^e mode in the m/z range of 50–800 Da, with an acquisition time of 0.1 s per scan.

The raw files were preprocessed by Progenesis QI software by Waters®, and identification was executed using multiple data banks. Identification of the metabolites of interest was carried out manually by spectral features, and the identification level 3 was obtained according to Schrimpe-Rutledge et al. [36] using 5ppm as the error cutoff. The integration area of each peak was used to calculate the violin plot graph and an unpaired t-test with Welch's correction was used for statistical comparison. All analysis were performed using GraphPad Prism 8.0 software (San Diego, CA, USA) and a significance level of $p \leq 0.05$ was adopted.

RNA extraction, gene expression analysis and viral load

Total RNA extraction was performed using TRI Reagent according to the manufacturer's instructions (Sigma, St Louis, USA). RNA concentration was determined by a DeNovix spectrophotometer and RNA integrity was assessed by visualization of 28S and 18S ribosomal RNA on a 1% agarose gel. Reverse transcription was performed with 0.5 µg of RNA using a GoScript Reverse Transcriptase Kit (Promega, Madison, WI, USA) according to the manufacturer's instructions. qPCR was performed using astrocyte cDNA diluted 1:10 and the qPCR SybrGreen Supermix (Qiagen, Valencia, CA, USA) containing forward and reverse primers in RNAse-free water. All reactions were performed in a CFX384 Touch Real-Time PCR Detection System (Biorad, Hercules, CA, USA) and cycling conditions were set as follows: 50°C for 2 min; 95°C for 10 min; (95°C for 15s; 60°C for 1 min) x 40 cycles. To evaluate primer

specificity, a melting curve analysis was performed by heating samples from 65°C to 99°C (1°C increment changes at 5s intervals). All sample measurements were performed in duplicate. Primers were designed with PrimerBlast and used at the concentration of 200 nM. Data were normalized to the expression of 18S (Fwd 5' CCCAACTTCTTAGAGGGACAAG 3'; Rev 5' CATCTAAGGGCATCACAGACC 3') and the relative quantification value of each target gene was determined using a comparative CT method [37]. For virus detection, SARS-CoV-2 nucleocapsid N1 primers were used as previously described (Fwd 5' CAATGCTGCAATCGTGCTAC 3'; Rev 5' GTTGCGACTACGTGATGAGG 3') [38,39]. A serial dilution of SARS-CoV-2 was used as a standard curve. Data were expressed as mean ± SEM. Statistical significance analysis was calculated by two-tailed unpaired Student's t-test. All analysis were performed using GraphPad Prism 8.0 (San Diego, CA, USA) and a significance level of $p \leq 0.05$ was adopted.

Astrocyte bioenergetics

Astrocytes were plated on Seahorse XF-24 plates at a density of $1.5x10^4$ cells per well and incubated in complete culture medium for two days at 37°C in 5% CO_2. 24 hours before the experiment, cells were either infected by SARS-CoV-2 (MOI 0.1) or not infected (MOCK). One day post-infection, the culture medium was changed to Seahorse Base medium (supplemented with 1 mM pyruvate, 2 mM glutamine, and 10 mM glucose) and cells were incubated at 37°C in a non-CO_2 incubator for 1 hour. OCR (Oxygen Consumption Rate) was measured over the course of the experiment under basal conditions and after the injections of oligomycin (1 µM), FCCP (5 µM) and antimycin A/rotenone (100 nM/1 µM). Protein concentration was determined for each well to normalize the data. Data were expressed as mean ± SEM of at least two independent experiments performed in quintuplicate. Statistical significance analysis was

calculated by two-tailed unpaired Student's t-test. All analysis were performed using GraphPad Prism 8.0 software (San Diego, CA, USA) and a significance level of $p \leq 0.05$ was adopted.

SH-SY5Y culture in astrocytes conditioned medium

Astrocytes and SH-SY5Y cells were cultured separately in standard conditions until complete differentiation. Next, astrocytes were infected either with MOCK or SARS-CoV-2 (MOI 0.1) and after 24 hours, the medium was removed and cells were washed with PBS and cultured for 24 hours. The SH-SY5Y medium was removed and replaced by astrocyte-conditioned medium and cells were incubated for 24 hours. After incubation, cells and the medium were collected for Flow Cytometer Analysis, following the described procedure below.

Flow cytometer analysis

SH-SY5Y cell viability was determined 24 h after incubation with astrocyte-conditioned medium. The percentage of live cells (Apotracker-/FVS510-) or early (Apotracker+/FVS510-) and late (Apotracker+/FVS510+) apoptotic cells was determined by flow cytometry (FACSymphony -Becton & Dickinson, San Diego, CA, USA), after labeling with fixable viability stain (FVS510, BD Biosciences, #564406) and ApotrackerTM Green (BioLegend, #427403). Data were analyzed using FlowJo software (BD Biosciences). Data are representative of at least two independent experiments performed in triplicate and are shown as mean ± SEM. P values were determined by ANOVA one-way followed by Tukey's post hoc test.

Lactate assay

Astrocyte supernatants from infected or non-infected cells were collected and deproteinized using 1 M perchloric acid (PCA) for 1 hour. Protein precipitation was performed by centrifugation at 18,000 xg for 5 minutes. pH was neutralized using KOH and lactate concentration was determined using a colorimetric L-lactate assay kit (cat. no. 138; Labtest). Data were expressed as mean ± SEM of at least two independent experiments performed in triplicate. Statistical significance was calculated by two-tailed unpaired Student's t-test. All analysis were performed using GraphPad Prism 8.0 software (San Diego, CA, USA) and a significance level of $p \leq 0.05$ was adopted.

Data availability

The mass spectrometry proteomic data have been deposited to the ProteomeXchange Consortium via the PRIDE [40] partner repository with the dataset identifier PXD021812 and 10.6019/PXD021812.

Acknowledgements

We thank Edison Luiz Durigon for providing the SARS-CoV-2 299. We thank Gabriela Lopes Vitória, Elzira E. Saviani and Paulo Baldasso for technical support. The authors would like to thank FAPESP (São Paulo Research Foundation; grants 2020/04746-0; 2017/25588-1; 2019/00098-7; 2014/10068-4; 2020/04919-2; 2013/08216-2; 2020/05601-6; 2020/04860-8; 2019/11457-8; 2013/07559-3; 2013/07607-8), Fundo de Apoio ao Ensino, Pesquisa e Extensão (FAEPEX) Unicamp - Grant number: 2274/20, the Brazilian National Council for Scientific and

Technological Development - CNPq, and the Coordenação de Aperfeiçoamento de Pessoal de Nível Superior – Brazil (CAPES). The authors wish to thank Bradley J. Smith, MSc for English review support.

Author Contributions

F.C., V.C.C. and F.P.V. designed the majority of the experiments, performed the experiments, analyzed data and contributed to writing the manuscript. **P.H.V.** performed metabolomic analysis. **A.G.F.V., A.S.L.M.A., C.B-T., G.S.Z., G. R.-O., L.C.a, V.M.S-C., A.C. C.,** contributed to the study design, performed experiments and data interpretation. **F.C., A.C.C., A.G.F.V., A.S.L.M.A., C.B-T., G.S.Z., V.M.S-C.,** performed cell culture care and cell differentiation, flow cytometry and RT-PCRs analysis. **A.S.L.M.A., A.C.C., P.L.P., D.A.T.T., G.F.S., S.P.M., R.G.L., J.F., M.R., N.B.S., M. C.M., R.E.M.P.S.,** performed SARS-CoV-2 In vitro infections and BSL-3 work. **R.G.L., G.P.R., T.L.K., G.G.D., J.A.G., P.B.R., N.B.S.** performed experiments and discussed the data. **V.C.C., G.R.O., L.C.,** performed all proteomic experiments and systems biology analysis in silico. **R.B.J., L.S.S., M.H.N., I.K.A., M.R.B., M.K.M.A., J.R.S.J., L.L.D., M.E.P.C.S., I.M.P.S., E.D.R., S.M.G., L.H.L.S., V.B., B.M.C., F.C. and C.L.Y.** recruited patients, performed brain imaging and clinical assessments; **G.L.** performed statistical analysis. **T.M., A.D-N., L.F.F.S., M.D., P.S.** collected human *postmortem* brain samples, assessed clinical files and discussed the data. **M.N.B., S.B., L.S., A.F.** collected human *postmortem* brain samples and performed histological analysis. **F.P.V., B.M.S.M., G.M.A., E.M.S.F., J.C.A-F., E.A., A.S., F.Q.C., T.M.C.** performed immunofluorescence analysis, RT-PCR analysis, histological and morphological analysis. **A.S.V., A.D., M.A.R.V., C.D.M., S.K.R., A.S.F., P.M.M.M-V., J.L.P.M.,** conceived experiments, data interpretation, provided material and revised the paper. **M.A.M., T.M.C., D.M.S.,** provided the funding for

the study; formulated the hypothesis, designed experiments, analyzed data and wrote the manuscript with input from all authors. **D.M.S., T.M.C.** conceived and supervised the study.

DECLARATION OF INTERESTS

Authors declare no competing interests

References

1. Yang, X. *et al.* Clinical course and outcomes of critically ill patients with SARS-CoV-2 pneumonia in Wuhan, China: a single-centered, retrospective, observational study. *Lancet Respir Med* **8**, 475–481 (2020).
2. Kotfis, K. *et al.* COVID-19: ICU delirium management during SARS-CoV-2 pandemic. *Crit. Care* **24**, 176 (2020).
3. Mao, L. *et al.* Neurologic Manifestations of Hospitalized Patients With Coronavirus Disease 2019 in Wuhan, China. *JAMA Neurol.* **77**, 683–690 (2020).
4. Varatharaj, A. *et al.* Neurological and neuropsychiatric complications of COVID-19 in 153 patients: a UK-wide surveillance study. *Lancet Psychiatry* **7**, 875–882 (2020).
5. Lu, Y. *et al.* Cerebral Micro-Structural Changes in COVID-19 Patients - An MRI-based 3-month Follow-up Study. *EClinicalMedicine* **25**, 100484 (2020).
6. De Felice, F. G., Tovar-Moll, F., Moll, J., Munoz, D. P. & Ferreira, S. T. Severe Acute Respiratory Syndrome Coronavirus 2 (SARS-CoV-2) and the Central Nervous System. *Trends Neurosci.* **43**, 355–357 (2020).
7. Biega, T. J., Lonser, R. R. & Butman, J. A. Differential cortical thickness across the central sulcus: a method for identifying the central sulcus in the presence of mass effect and vasogenic edema. *AJNR Am. J. Neuroradiol.* **27**, 1450–1453 (2006).

8. Li, B. *et al.* Prevalence and impact of cardiovascular metabolic diseases on COVID-19 in China. *Clin. Res. Cardiol.* **109**, 531–538 (2020).

9. Kovalevich, J. & Langford, D. Considerations for the use of SH-SY5Y neuroblastoma cells in neurobiology. *Methods Mol. Biol.* **1078**, 9–21 (2013).

10. Troyer, E. A., Kohn, J. N. & Hong, S. Are we facing a crashing wave of neuropsychiatric sequelae of COVID-19? Neuropsychiatric symptoms and potential immunologic mechanisms. *Brain Behav. Immun.* **87**, 34–39 (2020).

11. Rogers, J. P. *et al.* Psychiatric and neuropsychiatric presentations associated with severe coronavirus infections: a systematic review and meta-analysis with comparison to the COVID-19 pandemic. *Lancet Psychiatry* **7**, 611–627 (2020).

12. Song, E. *et al.* Neuroinvasion of SARS-CoV-2 in human and mouse brain. *bioRxiv* (2020) doi:10.1101/2020.06.25.169946.

13. Matschke, J. *et al.* Neuropathology of patients with COVID-19 in Germany: a post-mortem case series. *Lancet Neurol.* (2020) doi:10.1016/S1474-4422(20)30308-2.

14. Jacob, F. *et al.* Human Pluripotent Stem Cell-Derived Neural Cells and Brain Organoids Reveal SARS-CoV-2 Neurotropism. doi:10.1101/2020.07.28.225151.

15. Yavarpour-Bali, H. & Ghasemi-Kasman, M. Update on neurological manifestations of COVID-19. *Life Sci.* **257**, 118063 (2020).

16. Turner, D. A. & Adamson, D. C. Neuronal-astrocyte metabolic interactions: understanding the transition into abnormal astrocytoma metabolism. *J. Neuropathol. Exp. Neurol.* **70**, 167–176 (2011).

17. Walls, A. B. *et al.* Knockout of GAD65 has major impact on synaptic GABA synthesized from astrocyte-derived glutamine. *J. Cereb. Blood Flow Metab.* **31**, 494–503 (2011).

18. Bélanger, M., Allaman, I. & Magistretti, P. J. Brain energy metabolism: focus on astrocyte-neuron metabolic cooperation. *Cell Metab.* **14**, 724–738 (2011).

19. Bak, L. K., Schousboe, A. & Waagepetersen, H. S. The glutamate/GABA-glutamine cycle: aspects of transport, neurotransmitter homeostasis and ammonia transfer. *Journal of Neurochemistry* vol. 98 641–653 (2006).

20. Bonansco, C. *et al.* Glutamate released spontaneously from astrocytes sets the threshold for synaptic plasticity. *European Journal of Neuroscience* vol. 33 1483–1492 (2011).

21. Milad, M. R. & Rauch, S. L. The role of the orbitofrontal cortex in anxiety disorders. *Ann. N. Y. Acad. Sci.* **1121**, 546–561 (2007).

22. Knutson, K. M. *et al.* Areas of Brain Damage Underlying Increased Reports of Behavioral Disinhibition. *J. Neuropsychiatry Clin. Neurosci.* **27**, 193–198 (2015).

23. Mao, X.-Y. & Jin, W.-L. The COVID-19 Pandemic: Consideration for Brain Infection. *Neuroscience* **437**, 130–131 (2020).

24. Whelan, C. D. *et al.* Structural brain abnormalities in the common epilepsies assessed in a worldwide ENIGMA study. *Brain* **141**, 391–408 (2018).

25. Garcia, D. D. S. *et al.* Anxiety and depression symptoms disrupt resting state connectivity in patients with genetic generalized epilepsies. *Epilepsia* **60**, 679–688 (2019).

26. Bolognani, S. A. P. *et al.* Development of alternative versions of the Logical Memory subtest of the WMS-R for use in Brazil. *Dement. neuropsychol.* **9**, 136–148 (2015).

27. Campanholo, K. R. *et al.* Performance of an adult Brazilian sample on the Trail Making Test and Stroop Test. *Dement Neuropsychol* **8**, 26–31 (2014).

28. Jackson, C. The Chalder Fatigue Scale (CFQ 11). *Occup. Med.* **65**, 86 (2015).

29. Righart, R. *et al.* Volume versus surface-based cortical thickness measurements: A

comparative study with healthy controls and multiple sclerosis patients. *PLoS One* **12**, e0179590 (2017).

30. Genovese, C. R., Lazar, N. A. & Nichols, T. Thresholding of statistical maps in functional neuroimaging using the false discovery rate. *Neuroimage* **15**, 870–878 (2002).
31. Destrieux, C., Fischl, B., Dale, A. & Halgren, E. Automatic parcellation of human cortical gyri and sulci using standard anatomical nomenclature. *Neuroimage* **53**, 1–15 (2010).
32. Team, R. C. RA language and environment for statistical computing. Versión 3.4. 3, Vienna, Austria, R Foundation for Statistical Computing. (2017).
33. Fraga, A. M. *et al.* Establishment of a Brazilian Line of Human Embryonic Stem Cells in Defined Medium: Implications for Cell Therapy in an Ethnically Diverse Population. *Cell Transplant.* **20**, 431–440 (2011).
34. Trindade, P. *et al.* Short and long TNF-alpha exposure recapitulates canonical astrogliosis events in human-induced pluripotent stem cells-derived astrocytes. *Glia* **68**, 1396–1409 (2020).
35. Distler, U., Kuharev, J., Navarro, P. & Tenzer, S. Label-free quantification in ion mobility–enhanced data-independent acquisition proteomics. *Nat. Protoc.* **11**, 795–812 (2016).
36. Schrimpe-Rutledge, A. C., Codreanu, S. G., Sherrod, S. D. & McLean, J. A. Untargeted Metabolomics Strategies-Challenges and Emerging Directions. *J. Am. Soc. Mass Spectrom.* **27**, 1897–1905 (2016).
37. Schmittgen, T. D. & Livak, K. J. Analyzing real-time PCR data by the comparative C(T) method. *Nat. Protoc.* **3**, 1101–1108 (2008).
38. Won, J. *et al.* Development of a Laboratory-safe and Low-cost Detection Protocol for

SARS-CoV-2 of the Coronavirus Disease 2019 (COVID-19). *Exp. Neurobiol.* **29**, 107–119 (2020).

39. Codo, A. C. *et al.* Elevated Glucose Levels Favor SARS-CoV-2 Infection and Monocyte Response through a HIF-1α/Glycolysis-Dependent Axis. *Cell Metab.* (2020) doi:10.1016/j.cmet.2020.07.007.

40. Perez-Riverol, Y. *et al.* The PRIDE database and related tools and resources in 2019: improving support for quantification data. *Nucleic Acids Research* vol. 47 D442–D450 (2019).

Legends

Figure 1: Altered cerebral cortical thickness is associated with neuropsychiatric symptoms in COVID-19 patients. a) Surface-based morphometry using high-resolution 3T MRI. Yellow represents areas of decreased cortical thickness: left lingual gyrus, calcarine sulcus (and cuneus), and olfactory sulcus (and rectus gyrus). Blue represents areas of increased cortical thickness: central sulcus (precentral and postcentral gyrus) and superior occipital gyrus. Representative image of the analysis of 81 subjects tested positive for SARS-CoV-2 who had mild respiratory symptoms and did not require hospitalization or oxygen support compared to 145 healthy volunteers (without diagnosis of COVID-19). The analysis was performed within a median interval of 54 days. b) Correlation between BAI performance and right orbital gyrus thickness. The data depicts Pearson's correlation coefficient. c) Correlation between TRAIL B performance and right gyrus rectus thickness. Data depict Pearson's correlation coefficient and region of interest in representative images.

Figure 2: SARS-CoV-2 infects the central nervous system, replicates in astrocytes and causes brain damage. a) Histopathological H&E images of *postmortem* brain tissue from individuals who died of COVID-19. Five out of 26 individuals showed signs of brain damage as represented in the images by I) areas of necrosis, cytopathic damage (I, i.e., enlarged, hyperchromatic, atypical-appearing nuclei), vessels with margination of leukocytes and thrombus (II), and immune cells infiltrate (III). Images were acquired with 400x magnification. Scale bar indicates 50 μm. b) Viral load in brain tissues from the five COVID-19 patients who manifested histopathological alteration in the brain as compared to samples from SARS-CoV-2-negative controls (n=5 per group). c) Representative confocal images of the brain tissue of one COVID-19 patient who manifested histopathological alterations. Immunofluorescence targeting glial fibrillary acidic protein (GFAP, red), double-stranded RNA (dsRNA, magenta), SARS-CoV-2-S (green), and nuclei (DAPI, blue). Images were acquired with 630x magnification. Scale bar indicates 50 μm. d) Percentage of SARS-CoV-2-S positive cells in this tissue. e) Percentage of GFAP-positive vs. negative among infected cells. Ten fields were analyzed. f) Pearson's correlation coefficient demonstrating colocalization of SARS-CoV-2-S and dsRNA within GFAP-positive cells. g) KEGG-enrichment analysis of differentially expressed proteins found in a comparison between *postmortem* brain tissue samples from 12 COVID-19 patients vs. 8 controls. h) Cell type-enrichment analysis using the same data set. Dot size represents the number of proteins related to the respective cell type and the p value adjusted by the false discovery rate (FDR).

Figure 3: SARS-CoV-2 infects and replicates in astrocytes *in vitro*. Human neural stem

cell-derived astrocytes were infected *in vitro* with SARS-CoV-2 (MOI 1) for 1 h, washed, and harvested 24 h after infection. a) Immunostaining for GFAP (red), double-stranded RNA (dsRNA, magenta), SARS-CoV-2-S (green), and nuclei (DAPI, blue). Images were acquired with 630x magnification. Scale bar indicates 50 µm. b) SARS-CoV-2 viral load detection in astrocyte cell pellet (n = 15 replicates) using RT-PCR. c) Percentage of infected astrocytes. The data depicts SARS-CoV-2-S and DAPI stained cells (100 fields were analyzed). d) Frequency of cells containing replicating viruses. The data represents the percentage of dsRNA-stained cells into SARS-CoV-2-S positive cells (8 fields were analyzed). Data are representative of at least two independent experiments and shown as mean ± SEM. P values were determined by two-tailed unpaired with Welch's correction (b and d) **P < 0.01; **** P < 0.0001 compared to mock.

Figure 4: SARS-CoV-2 infection alters astrocyte metabolism and elicits a secretory phenotype that impairs neuronal viability. Human neural stem cell-derived astrocytes were infected *in vitro* with SARS-CoV-2 (MOI 0.1) for 1 h, washed thoroughly and harvested after 24 h. Mock was used as a control. a) Hierarchical clustering of differentially expressed proteins. b) Reactome functional interaction network of differentially expressed proteins. Colors show modules related to SARS-CoV-2 affected pathways ($p < 0.05$ calculated based on binomial test). c) KEGG-enrichment analysis of differentially expressed proteins in SARS-CoV-2 infected astrocytes vs. mock as compared to *postmortem* brain tissue from COVID-19 patients vs. controls. Dot size represents the number of proteins related to the respective cell type and the p value adjusted by the false discovery rate (FDR). d) High-resolution mass spectrometry quantification of pyruvate, lactate, glutamine, glutamate, GABA, and a-ketoglutarate in

SARS-CoV-2 infected astrocytes vs. mock. The integration area of each peak was used to calculate the violin plot graph and unpaired t-test with Welch's correction was used for statistical comparison. e) Oxygen consumption rate (OCR) of SARS-CoV-2 infected astrocytes vs. mock. SeaHorse Flux Analysis using the MitoStress test where basal respiration was measured followed by determination of oligomycin-, FCCP-, and rotenone/antimycin-induced respiration. f) Human neuronal cell line SH-SY5Y was cultured for 24 h in the presence of astrocyte-conditioned media (ACM) from mock or SARS-CoV-2 (CoV-2) infected cells. Representative histograms of cell apoptosis as measured by ApotrackerGreen staining. Data are representative of at least two independent experiments performed in triplicate (flow cytometry and metabolomics analysis) or quintuplicate (SeaHorse Flux Analysis), and shown as mean ± SEM. P values were determined by two-tailed unpaired with Welch's correction (c and d) and one-way ANOVA followed by Tukey's post hoc test (e). *$P < 0.05$; **$P < 0.01$; **** $P < 0.0001$ compared to mock, and #$P < 0.05$ compared to CoV-2 (ACM+).

Supplementary Fig. 1: Frequency of individuals with neuropsychological symptoms. The subgroup of individuals who performed neuropsychological evaluation presented a median age of 37.8 years (range 21-63 years), 16 years of education (range 6-24 years), and 59 days of the interval from their diagnosis of COVID-19 (range 21-120 days). The median values of BDI (range 0-36), and also of BAI (0-45) were 6 points. The median score of CFQ-11 was 16 (range 0-32). a) Presence of anxiety (BAI) and depression (BDI) symptoms. b) Performance on the logical memory (LM) test (Wechsler Memory Scale) and cognitive function tests (TRAIL Making Test A and B).

Supplementary Fig. 2: SARS-CoV-2 infects neurons, but not microglia in the brain from COVID-19. a) Histopathological alterations revealed by H&E images of *postmortem* brain tissue from individuals who died of COVID-19. Samples from 26 individuals were analyzed and 5 showed alterations. Case 1: intraparenchymal cerebral vessel with margination of inflammatory cells through endotelium; Case 2: focal infiltration of inflammatory cells – diapedesis; Case 3: intraparenchymal vascular damage; Case 4: perivascular edema and senile corpora amylacea. b-c) Representative immunostaining and confocal analysis from brain slices from autopsies of COVID-19 patients (n=5). The image depicts staining for: b) nuclei (DAPI, blue), NeuN (red, neuron marker), dsRNA (magenta), and SARS-CoV-2-S (green); and c) nuclei (DAPI, blue), ionized calcium-binding adaptor molecule 1 (Iba1, red, microglia marker), dsRNA (magenta), and SARS-CoV-2-S (green). Images were acquired with 630x magnification. Scale bar indicates 50 µm.

Supplementary Fig. 3: Metabolomic analysis of SARS-CoV-2-infected astrocytes. High-resolution mass spectrometry quantification of citrate, palmitate, acetate, fumarate, succinate, oxaloacetate, and malate in SARS-CoV-2 infected astrocytes vs. mock. The integration area of each peak was used to calculate the violin plot graph and unpaired t-test with Welch's correction was used for statistical comparison.

Supplementary Fig. 4: Bioenergetics of SARS-CoV-2-infected astrocytes. Human neural stem cell-derived astrocytes were infected *in vitro* with SARS-CoV-2 (MOI 0.1) for 1 h, washed thoroughly and harvested after 24 h. Mock was used as a control. Oxygen consumption rate

(OCR) was assessed by SeaHorse Flux Analysis and cell respiration parameters were determined using the MitoStress test. Data are expressed as mean ± SEM of at least two independent experiments performed in quintuplicate. Statistical analysis was calculated by two-tailed unpaired Student's t-test. Data was normalized by protein content.

Supplementary Fig. 5: Lactate production by SARS-CoV-2-infected astrocytes. Human neural stem cell-derived astrocytes were infected *in vitro* with SARS-CoV-2 (MOI 0.1) for 1 h, washed thoroughly and lactate levels were measured in conditioned medium after 24 h. Mock was used as a control. Data are representative of at least three independent experiments and are shown as mean ± SEM.

a)

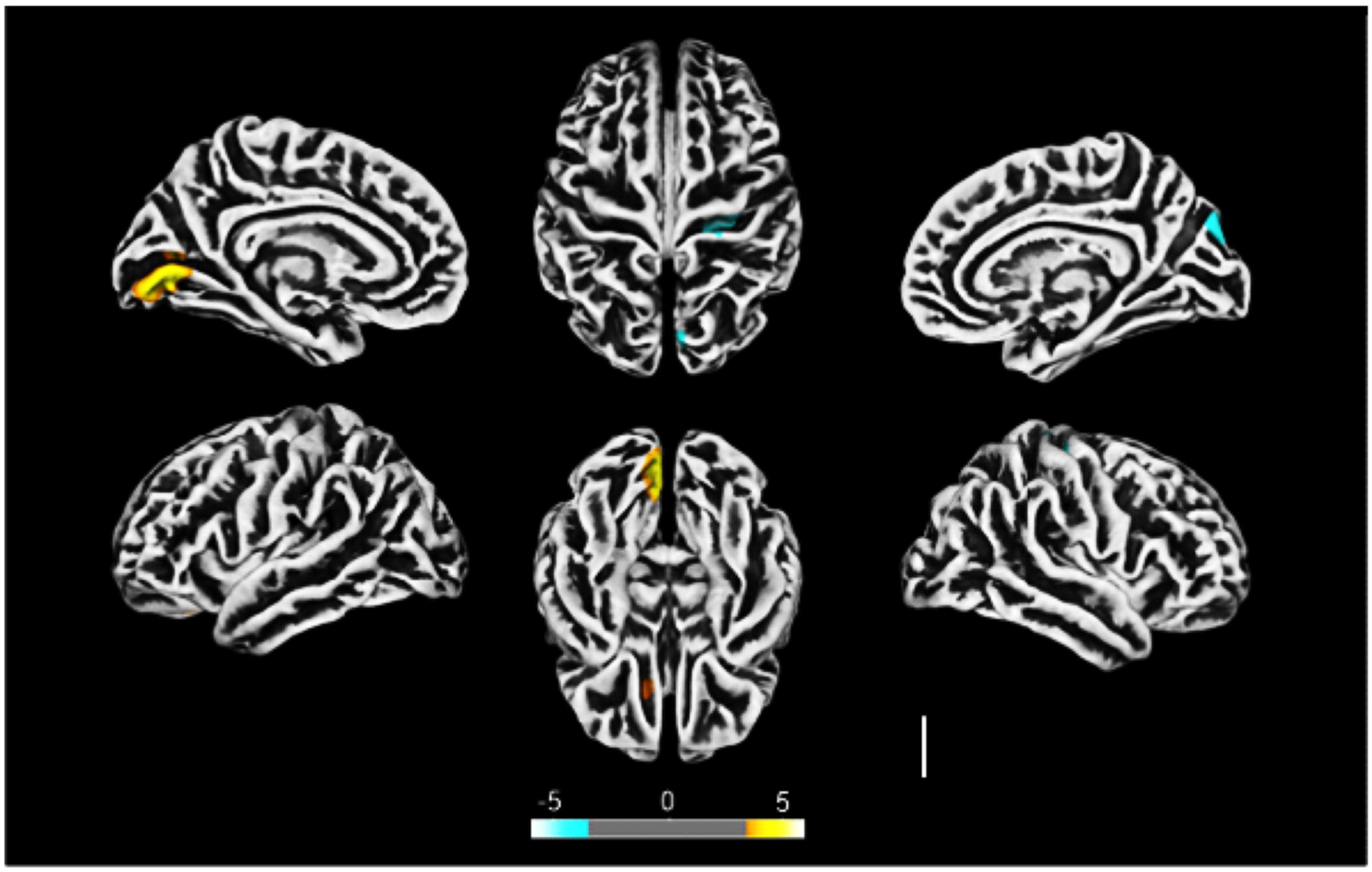

b)

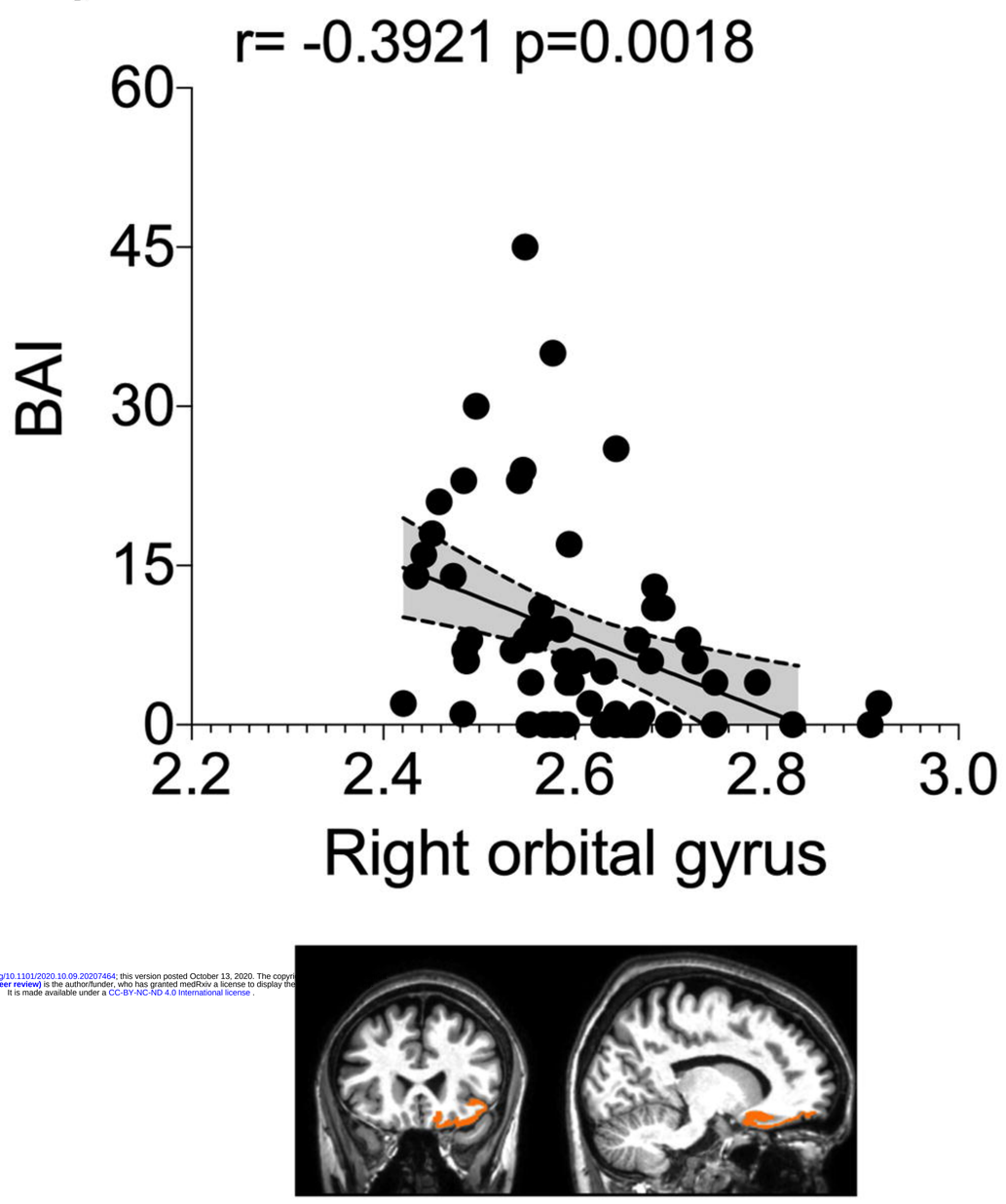

c)

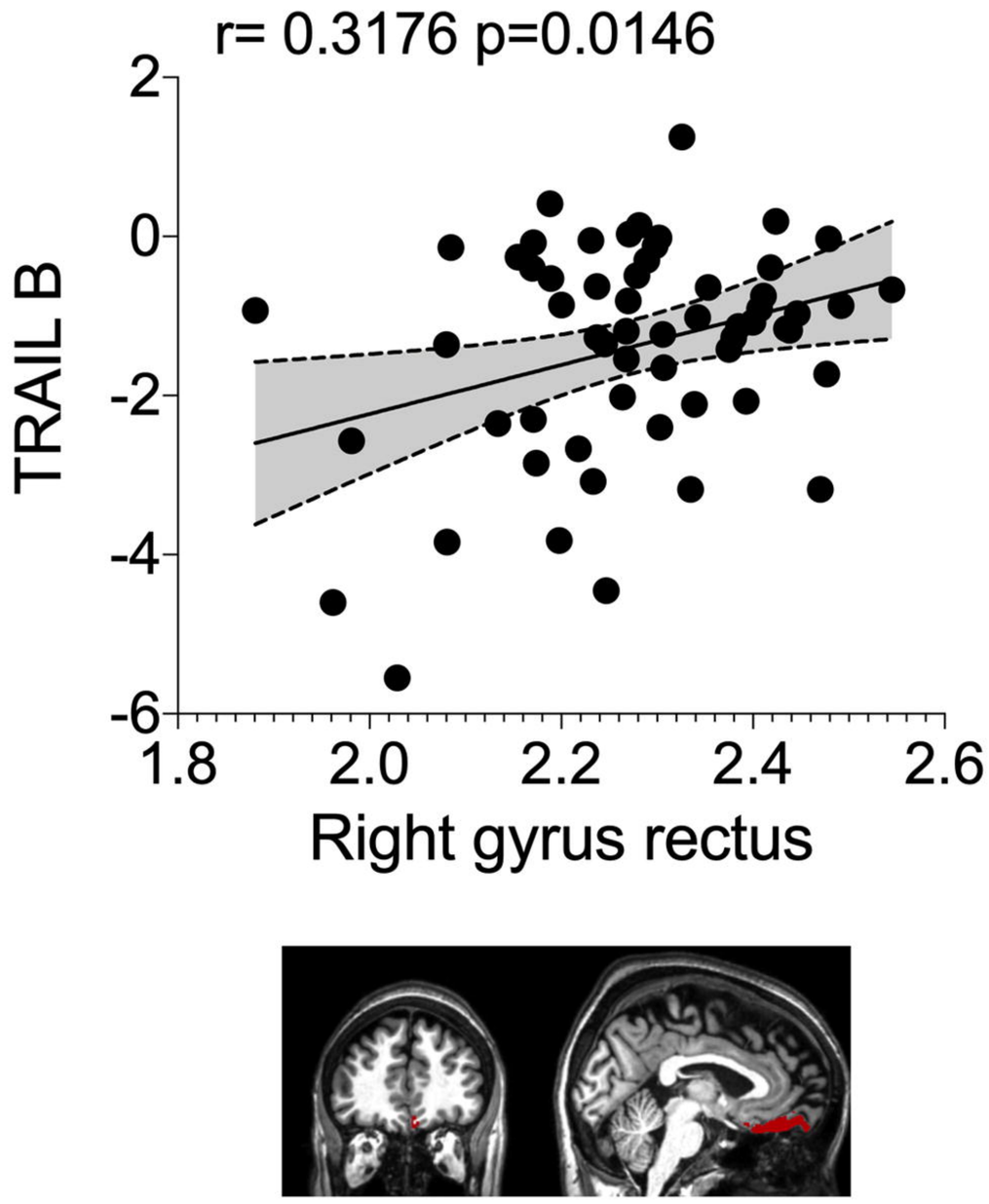

Figure 1

Figure 2

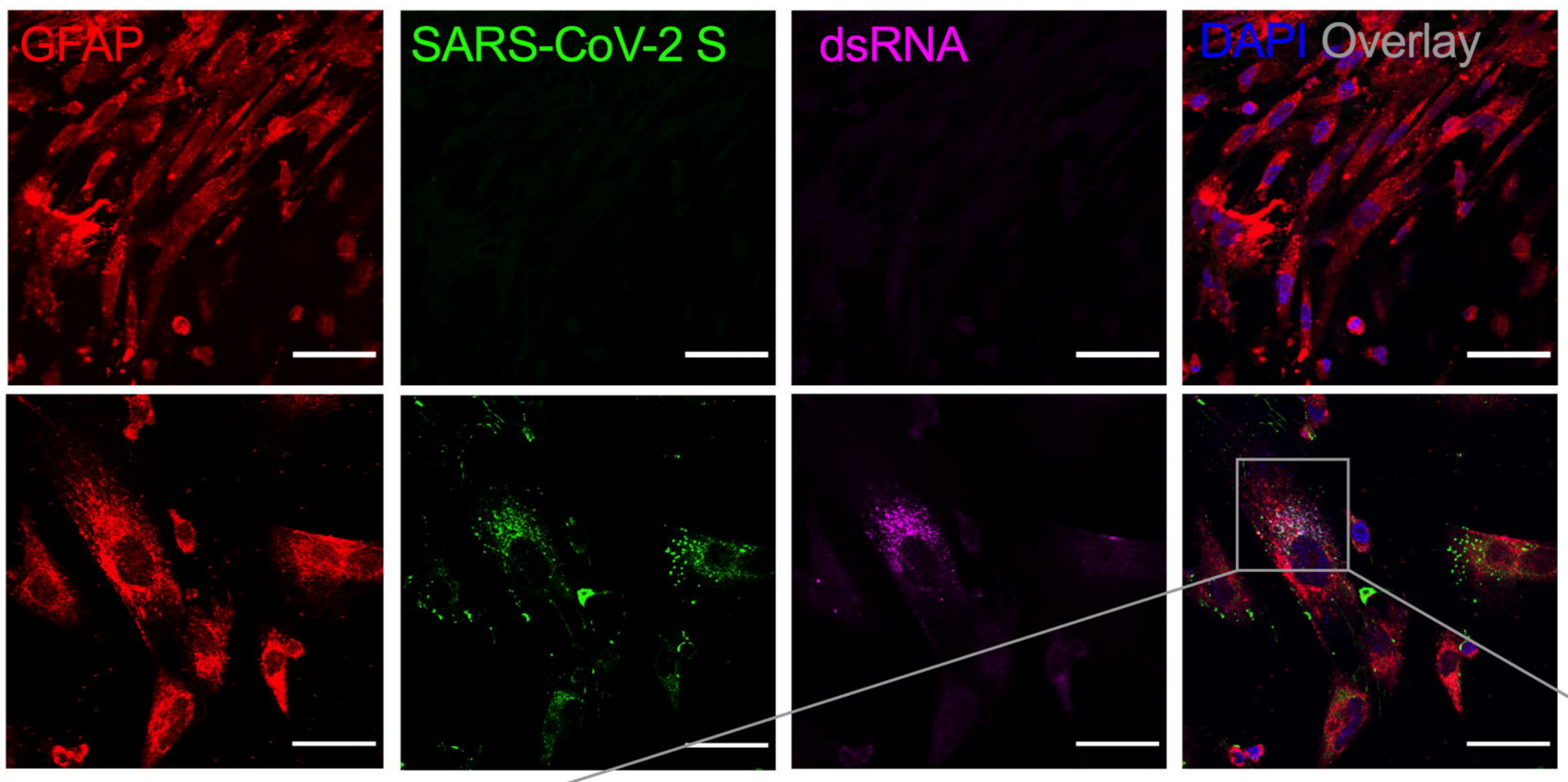

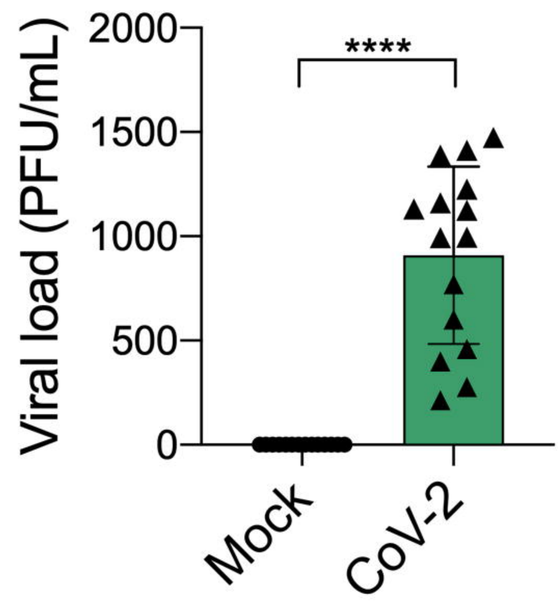

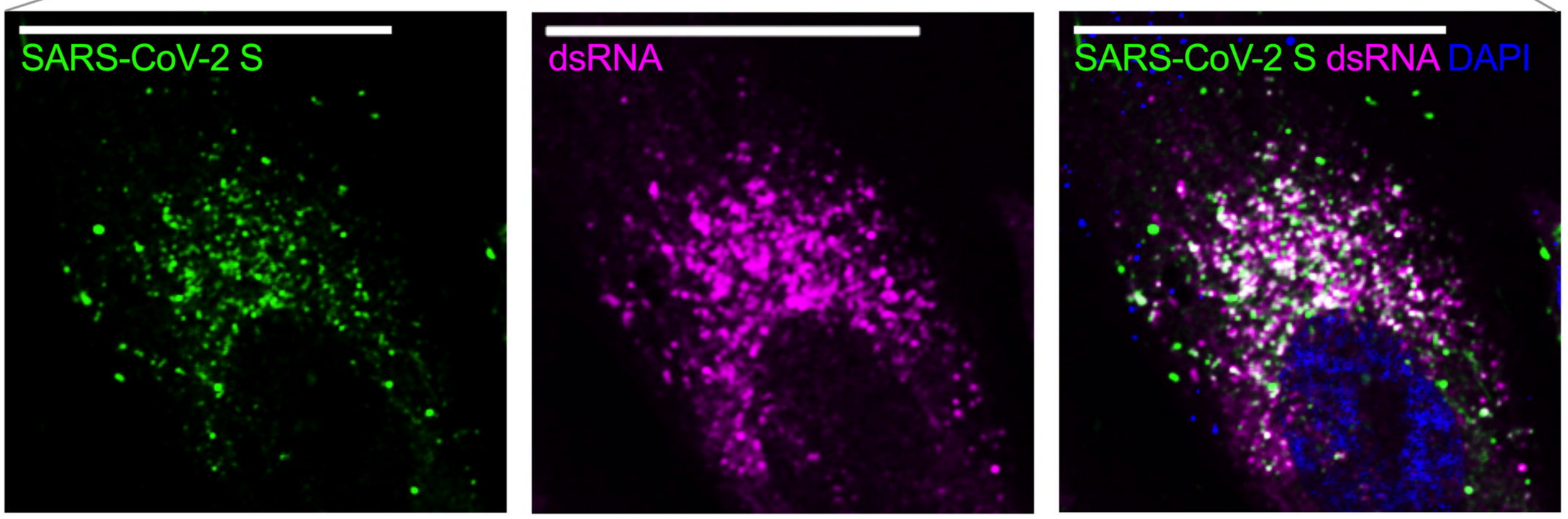

Figure 3

a)

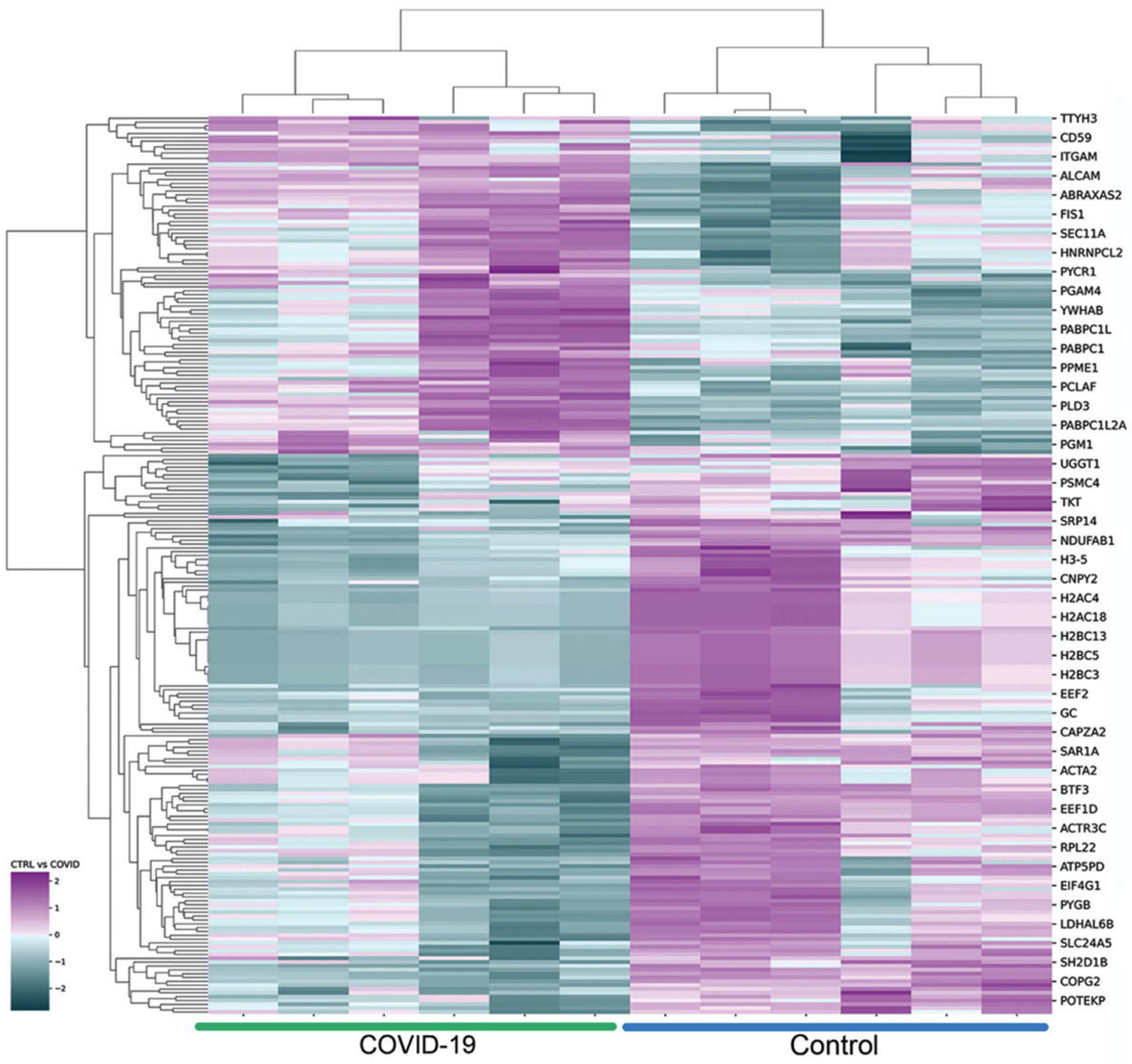

b)

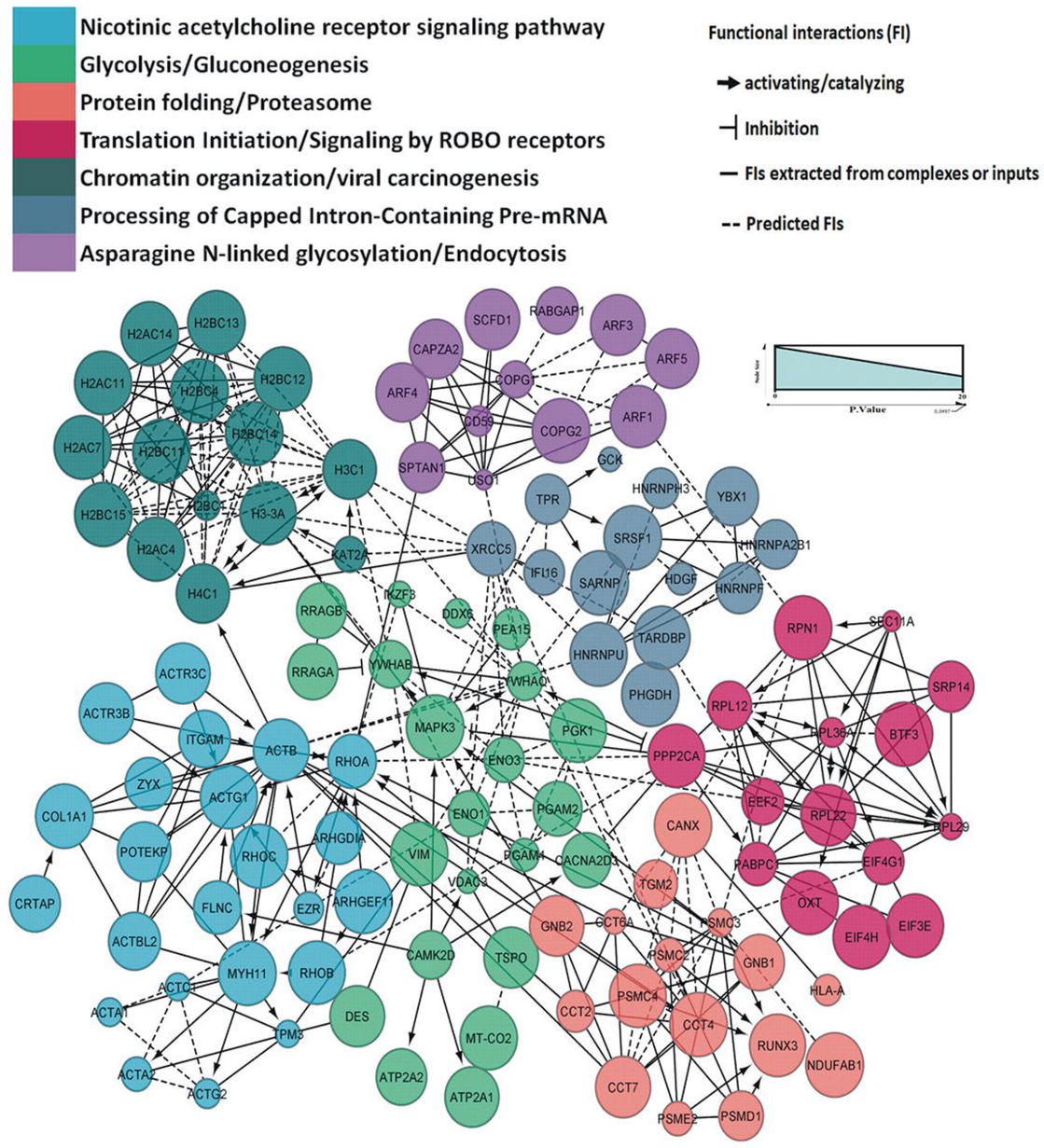

c)

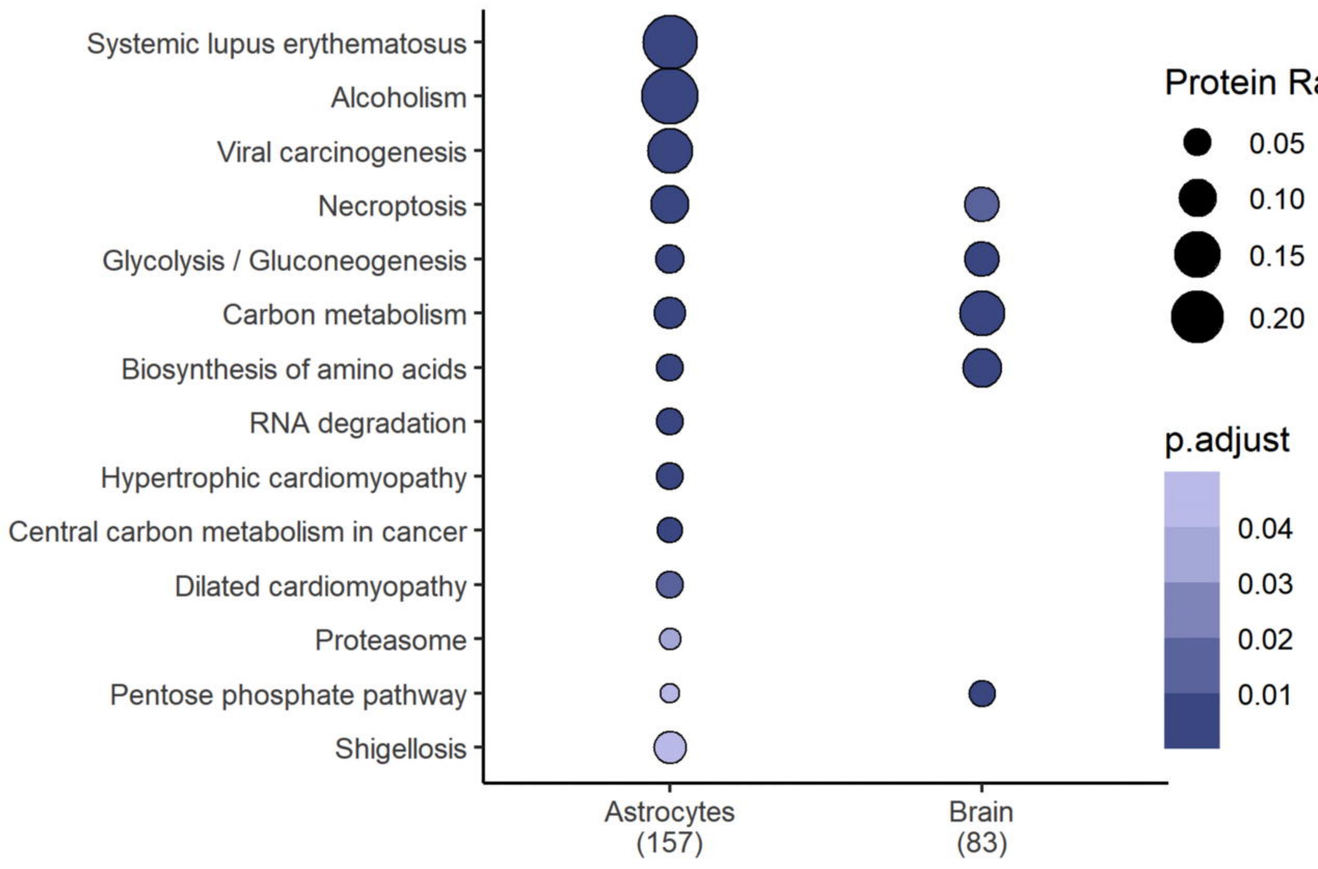

d)

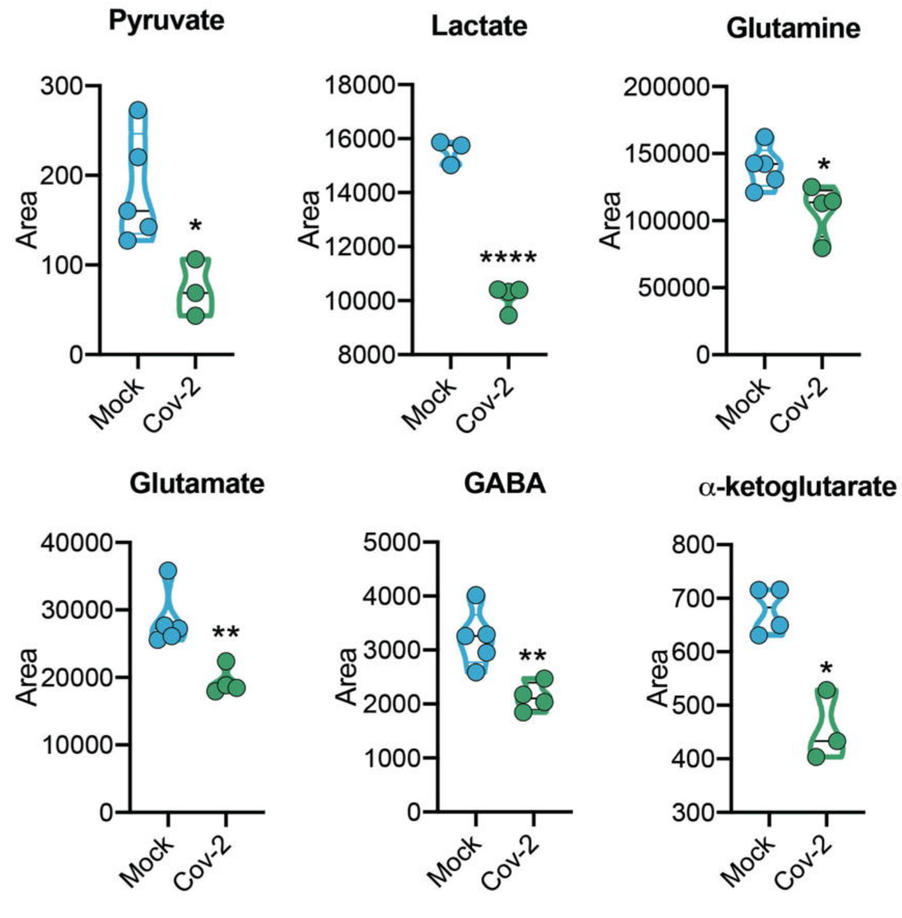

e)

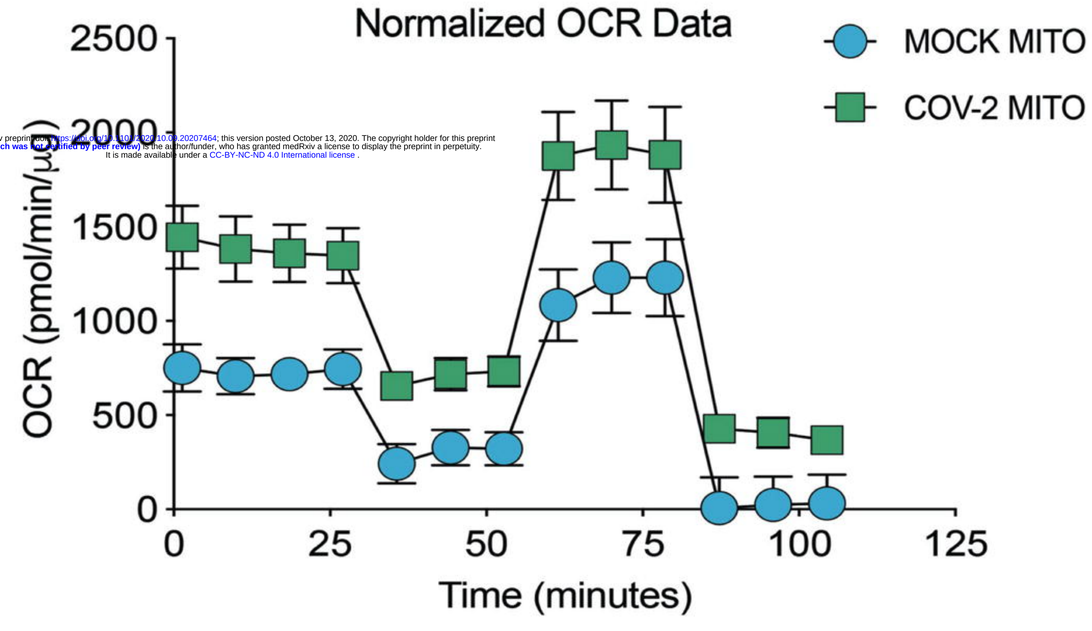

f)

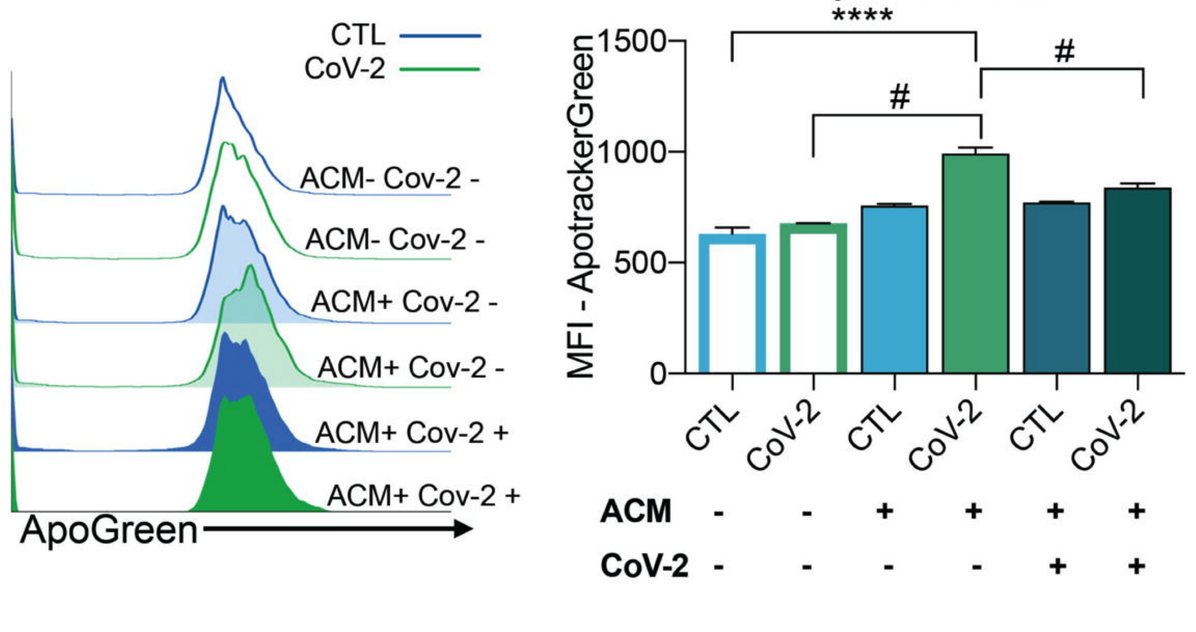

Figure 4

a)

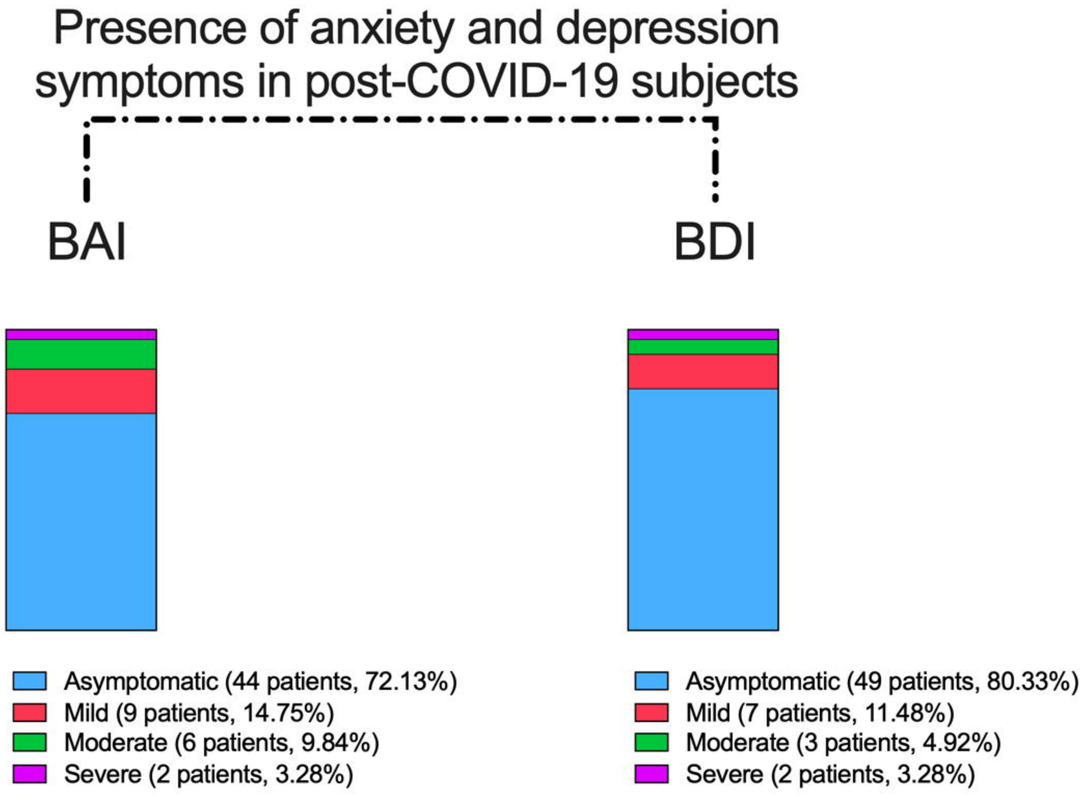

b)

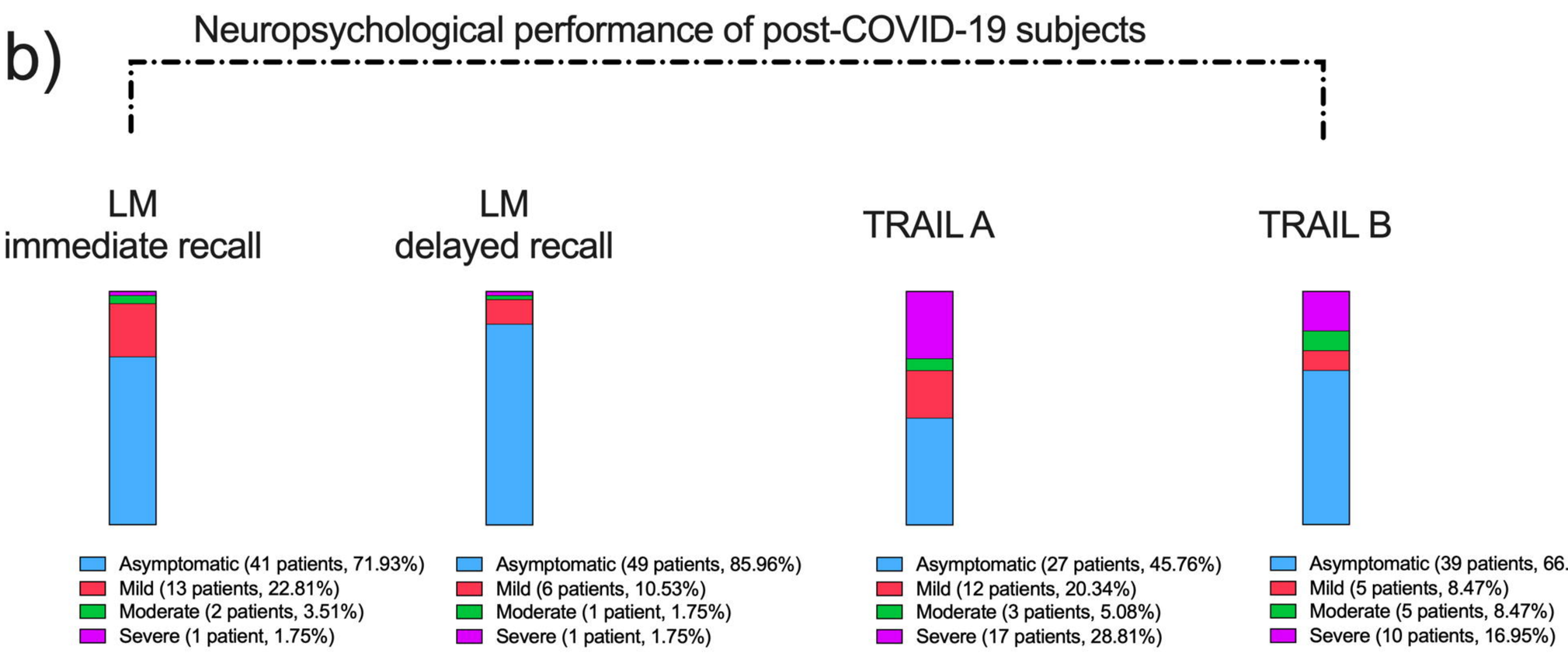

Supplementary Figure 1

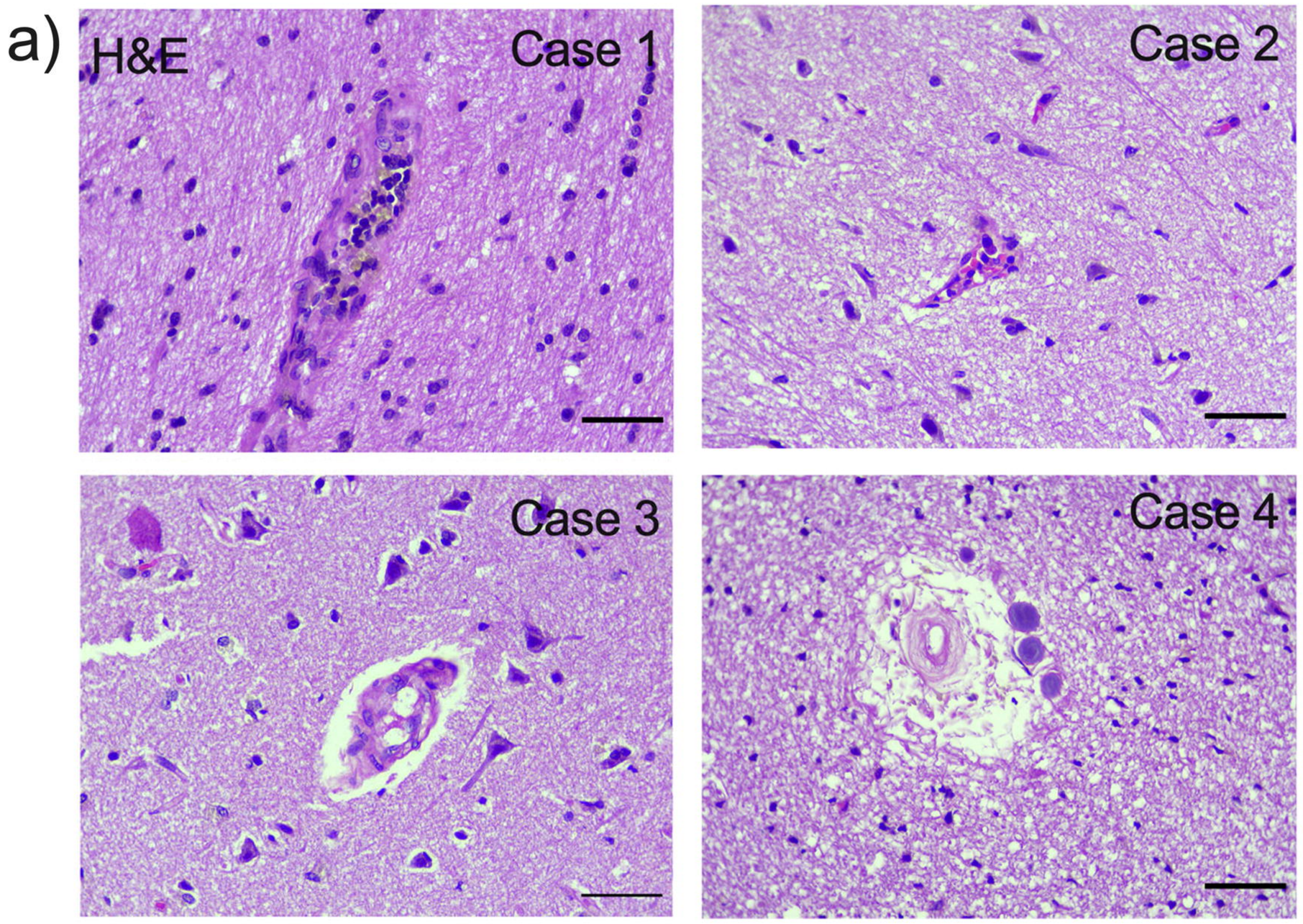

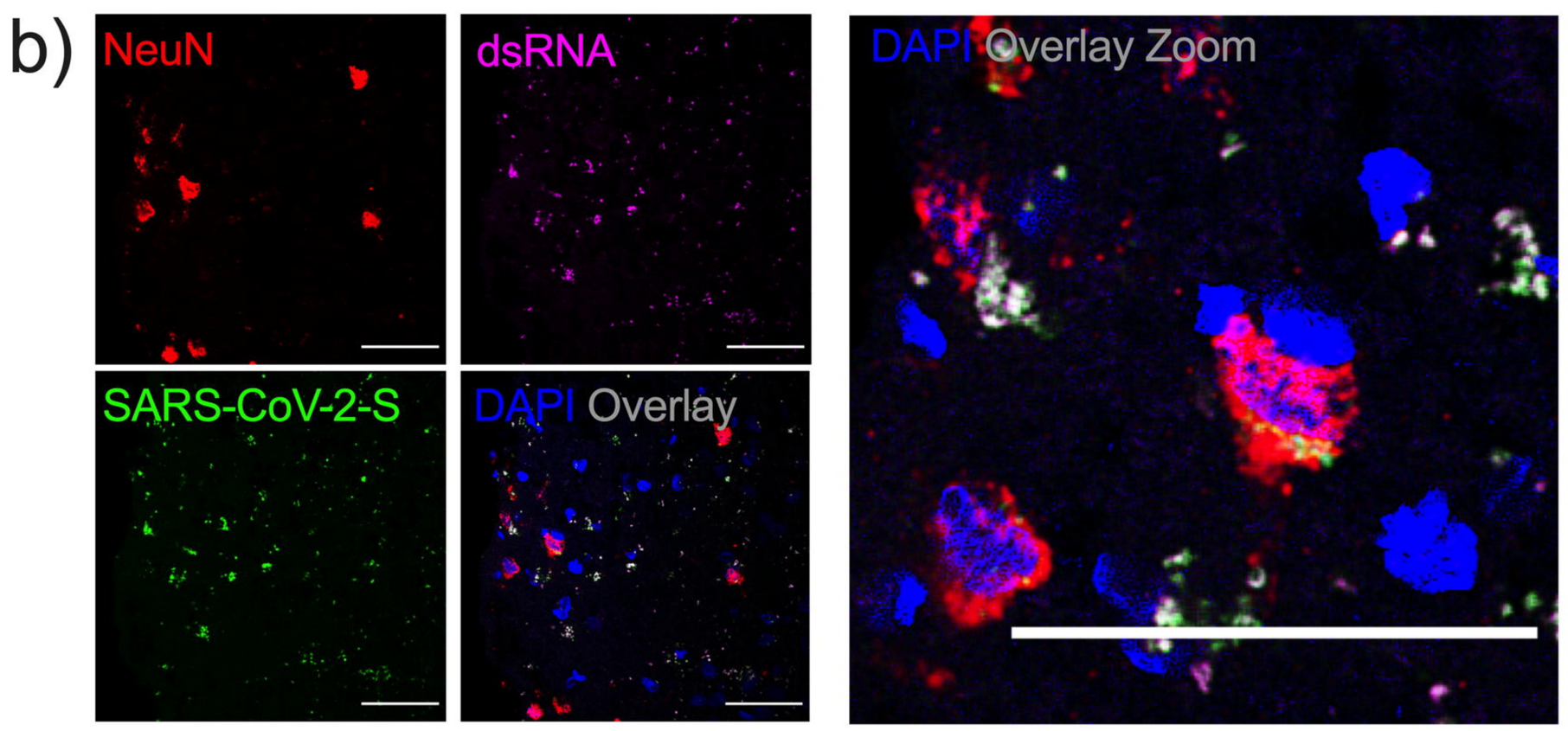

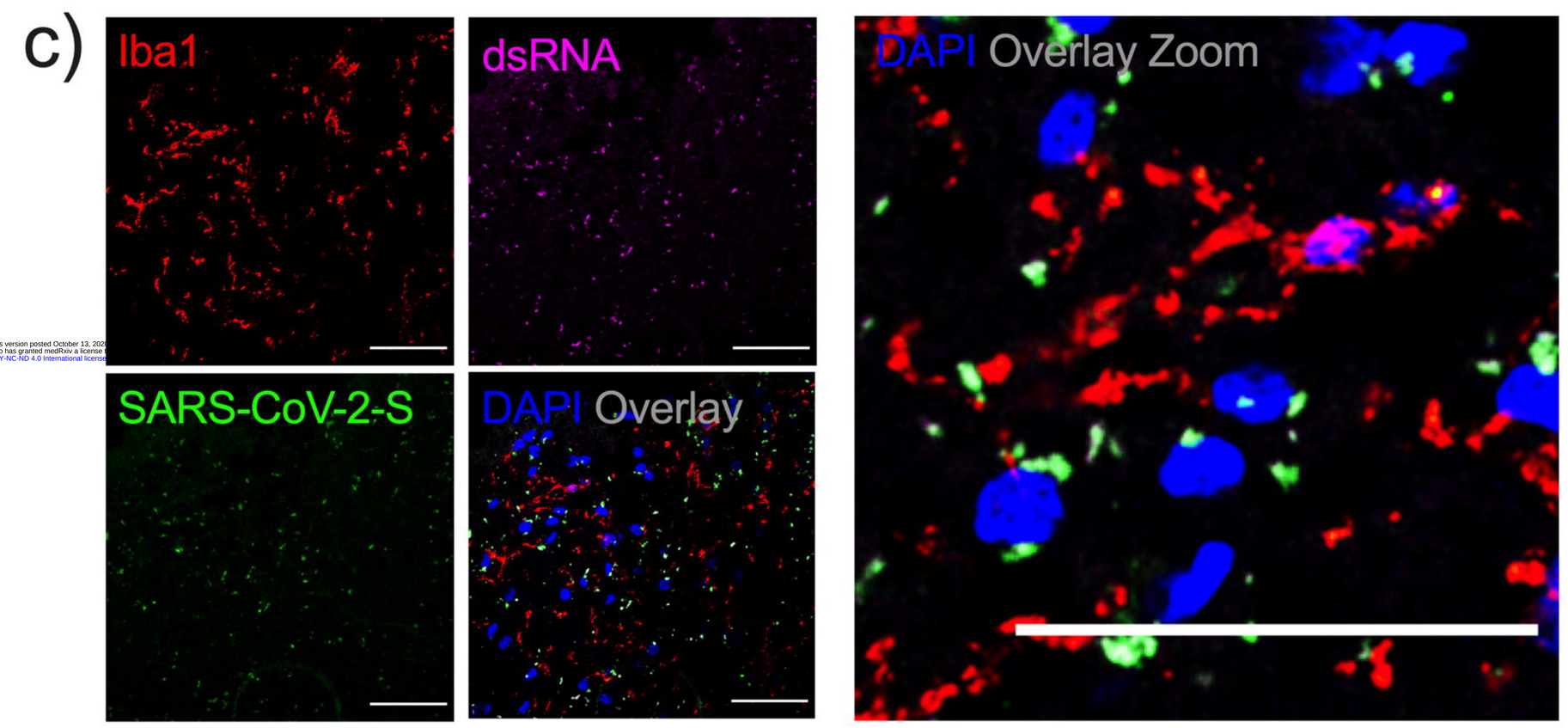

Supplementary Figure 2

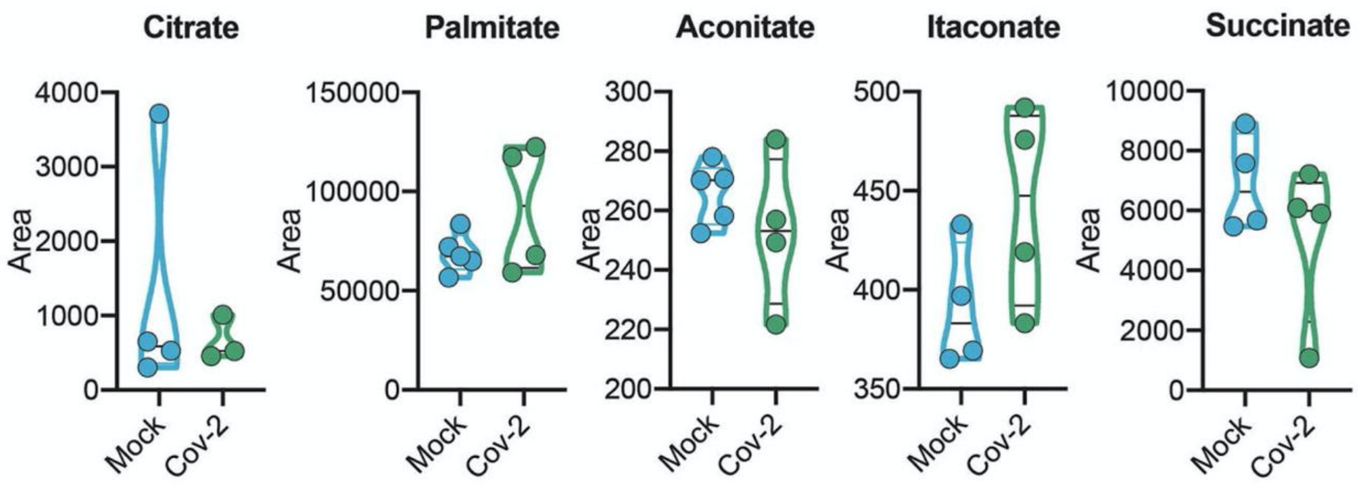

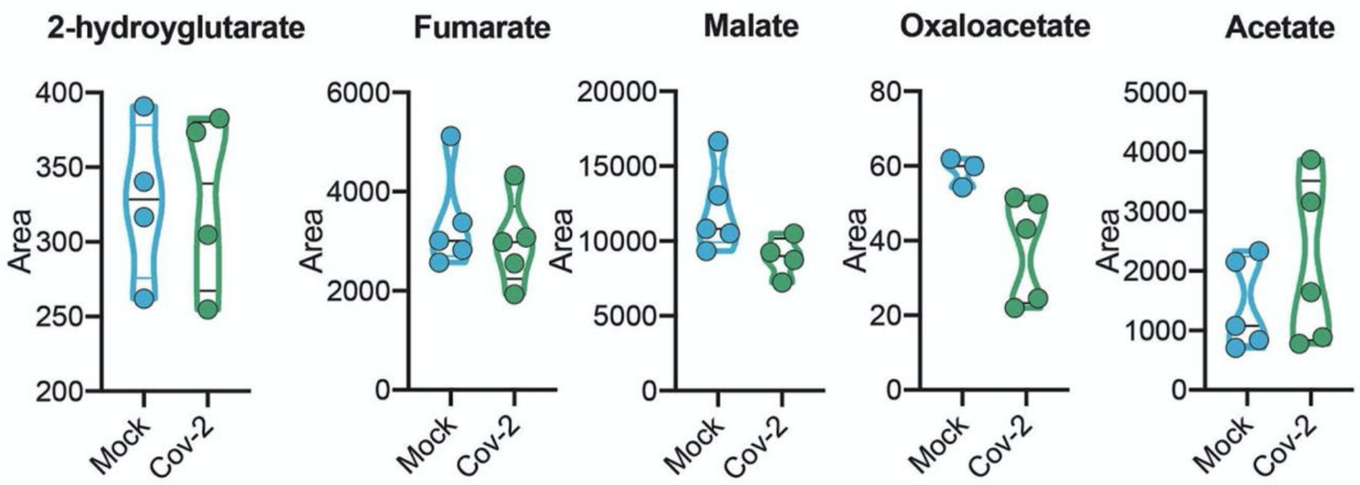

Supplementary Figure 3

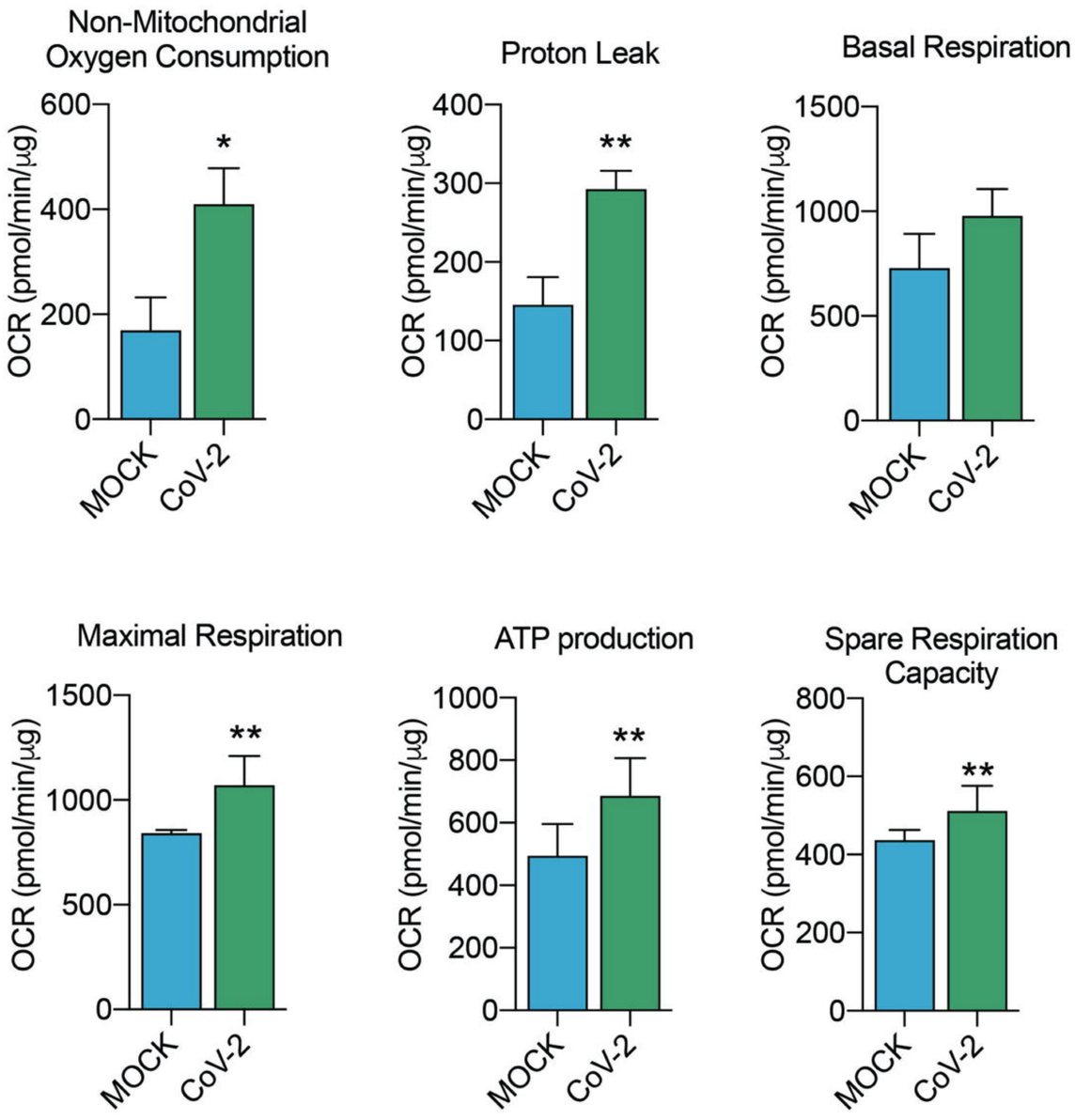

Supplementary Figure 4

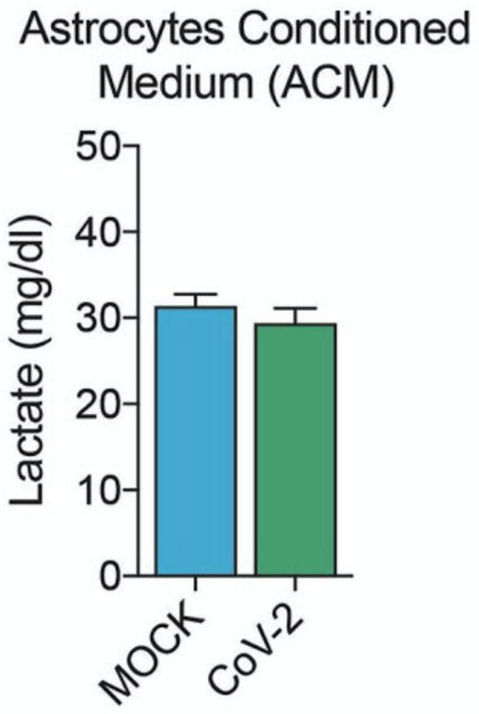

Supplementary Figure 5

Table 1. Reduced cortical thickness in the left hemisphere

Value (T statistic)	Cluster size (number of voxels)	Overlap of atlas region	Anatomical correspondence
5	193	G_oc-temp_med-Lingual	Lingual gyrus
4.6	77	S_calcarine	Calcarine sulcus
		G_cuneus	Cuneus
		S_parieto_occipital	Parieto-occipital sulcus
4	26	S_orbital_med-olfact	Olfactory sulcus
		G_rectus	Rectus gyrus

Table 2. Increased cortical thickness in the right hemisphere

Value (T statistic)	Cluster size (number of voxels)	Overlap of atlas region	Anatomical correspondence
5.4	277	S_central	Central sulcus
		G_precentral	Precentral gyrus
		G_postcentral	Postcentral gyrus
4.2	40	G_occipital_sup	Superior occipital gyrus
		G_cuneus	Cuneus

Table 3. Results of Neuropsychological tests (in z-score)

	Median	Range
Logical memory (immediate recall)	-0.63	-2.25 to 1.96
Logical memory (delayed recall)	-0.27	-2.37 to 1.58
TRAIL A	-0.7	-7 to 0.77
TRAIL B	-1.13	-5.55 to 1.25

Table 4. Correlations between BAI scores and cortical thickness of orbitofrontal regions

	Correlation	Significance	FDR adjusted significance
Left gyrus orbital	-0.19	0.2	0.4
Right gyrus orbital	-0.42	0.004	0.016
Left gyrus rectus	-0.017	0.91	0.91
Right gyrus rectus	-0.1	0.5	0.67

FDR: false discovery rate

Table 5. Correlations between TRAIL B scores and thickness of gyrus rectus

	Correlation	Significance	FDR adjusted significance
Left gyrus rectus	0.1	0.43	0.43
Right gyrus rectus	0.32	0.014	0.03

FDR: false discovery rate

Table 6. Correlations between Logical memory (immediate recall) scores and cortical thickness of IFG and STG.

	Correlation	Significance	FDR adjusted significance
Left IFG (pars opercularis)	0.27	0.08	0.1
Right IFG (pars opercularis)	0.28	0.07	0.1
Left IFG (pars triangularis)	0.35	0.02	0.04
Right IFG (pars triangularis)	0.43	0.004	0.02
Left STG (planum temporale)	0.39	0.01	0.03
Right STG (planum temporale)	0.25	0.12	0.12

IFG: inferior frontal gyrus; STG: superior temporal gyrus; FDR; false discovery rate